NAVAL POSTGRADUATE SCHOOL

MONTEREY, CALIFORNIA

THESIS

RESOLUTION OF PORT/STARBOARD AMBIGUITY USING A LINEAR ARRAY OF TRIPLETS AND A TWIN-LINE PLANAR ARRAY

by

Stilson Veras Cardoso

June 2016

Thesis Advisor:	Lawrence J. Ziomek
Second Reader:	Monique P. Fargues

Approved for public release; distribution is unlimited

THIS PAGE INTENTIONALLY LEFT BLANK

REPORT DOCUMENTATION PAGE

Form Approved OMB No. 0704-0188

1. AGENCY USE ONLY *(Leave blank)*	2. REPORT DATE June 2016	3. REPORT TYPE AND DATES COVERED Master's Thesis

4. TITLE AND SUBTITLE RESOLUTION OF PORT/STARBOARD AMBIGUITY USING A LINEAR ARRAY OF TRIPLETS AND A TWIN-LINE PLANAR ARRAY	5. FUNDING NUMBERS
6. AUTHOR(S) Stilson Veras Cardoso	

7. PERFORMING ORGANIZATION NAME(S) AND ADDRESS(ES) Naval Postgraduate School Monterey, CA 93943-5000	8. PERFORMING ORGANIZATION REPORT NUMBER

9. SPONSORING /MONITORING AGENCY NAME(S) AND ADDRESS(ES) N/A	10. SPONSORING/MONITORING AGENCY REPORT NUMBER

11. SUPPLEMENTARY NOTES The views expressed in this thesis are those of the author and do not reflect the official policy or position of the Department of Defense or the U.S. Government. IRB Protocol number _____N/A_____.

12a. DISTRIBUTION / AVAILABILITY STATEMENT Approved for public release; distribution is unlimited	12b. DISTRIBUTION CODE

13. ABSTRACT (maximum 200 words)

This thesis is a study on the ability of towed sonar arrays to resolve the PS (port/starboard) ambiguity problem, and focuses on a twin-line planar array and a linear array of triplets. A twin-line planar array is commonly employed in underwater warfare. The goal is to offer the reader a comprehensive understanding of the method used for the solution of the PS ambiguity problem, concerning the beamformer's complex weights, operating frequency and limit on beam steering.

Initially, the basic characteristics and functional blocks, technical and operational peculiarities of towed linear sonar arrays are presented, and then a single triplet, a linear array of triplets and a twin-line planar array are respectively examined in detail.

The research consists of mathematical modeling of the elements and the arrays, calculation of beam patterns for study cases, and signal processing simulations programmed in MATLAB. The simulations make use of a signal generator, designed to assess the performance of the twin-line planar array. The generator provides the reader with a systems view of the array operation, taking into account the characteristics of the target and medium.

14. SUBJECT TERMS towed sonar array, port/starboard ambiguity problem, single triplet, linear array of triplets, twin-line planar array	15. NUMBER OF PAGES 111
	16. PRICE CODE

17. SECURITY CLASSIFICATION OF REPORT Unclassified	18. SECURITY CLASSIFICATION OF THIS PAGE Unclassified	19. SECURITY CLASSIFICATION OF ABSTRACT Unclassified	20. LIMITATION OF ABSTRACT UU

NSN 7540-01-280-5500

Standard Form 298 (Rev. 2-89)
Prescribed by ANSI Std. 239-18

THIS PAGE INTENTIONALLY LEFT BLANK

RESOLUTION OF PORT/STARBOARD AMBIGUITY USING A LINEAR ARRAY OF TRIPLETS AND A TWIN-LINE PLANAR ARRAY

Stilson Veras Cardoso
Civilian, Brazilian Navy
B.S., University of Brasília, 1993

Submitted in partial fulfillment of the
requirements for the degree of

MASTER OF SCIENCE IN ENGINEERING ACOUSTICS

from the

**NAVAL POSTGRADUATE SCHOOL
June 2016**

Approved by: Dr. Lawrence J. Ziomek
                  Thesis Advisor

                  Dr. Monique P. Fargues
                  Second Reader

                  Dr. Daphne Kapolka
                  Chair, Engineering Acoustics Academic Committee

THIS PAGE INTENTIONALLY LEFT BLANK

ABSTRACT

This thesis is a study on the ability of towed sonar arrays to resolve the PS (port/starboard) ambiguity problem, and focuses on a twin-line planar array and a linear array of triplets. A twin-line planar array is employed in underwater surveillance. The goal is to offer the reader a comprehensive understanding of the method used for the solution of the PS ambiguity problem concerning the beamformer's complex weights, operating frequency and limit on beam steering.

Initially, the basic characteristics and functional blocks, and technical and operational peculiarities of towed linear sonar arrays, are presented, and then a single triplet, a linear array of triplets, and a twin-line planar array are respectively examined in detail.

The research consists of mathematical modeling of the elements and the arrays, calculation of beam patterns for study cases, and signal processing simulations programmed in MATLAB. The simulations make use of a signal generator designed to assess the performance of the twin-line planar array. The generator provides the reader with a systems view of the array operation, taking into account the characteristics of the target and medium.

THIS PAGE INTENTIONALLY LEFT BLANK

TABLE OF CONTENTS

LIST OF FIGURES

x

LIST OF TABLES

THIS PAGE INTENTIONALLY LEFT BLANK

LIST OF ACRONYMS AND ABBREVIATIONS

ATM	Asynchronous Transfer Mode
AWGN	additive white Gaussian noise
CW	continuous wave
DAC	digital-to-analog converter
DFT	discrete Fourier transform
DOA	direction of arrival
DSP	digital signal processing
DTMB	David Taylor Model Basin
FF	far-field
FORA	Five Octave Research Array
FFT	fast Fourier transform
HFM	hyperbolic frequency modulation
LFAS	low frequency active sonar
LFM	linear frequency modulation
NATO	North Atlantic Treaty Organization
NF	near-field
NURC	NATO Undersea Research Centre
ONR	Office of Naval Research
PS	port/starboard
RN	radiated noise
RNL	radiated noise level
RS	receiver sensitivity
RSL	receiver sensitivity level
SONET	Synchronous Optical Network
SPL	sound pressure level
UUV	unmanned undersea vehicle
WSS	wide-sense stationary

THIS PAGE INTENTIONALLY LEFT BLANK

ACKNOWLEDGMENTS

THIS PAGE INTENTIONALLY LEFT BLANK

PROLOGUE

"The Tamoio's Song"
(Encouraging words of a warrior of the Tamoio tribe to his newborn son)[*]

Weep not, my son
weep not, life is
a keen struggle.
To live is to strive
life is a fight
that brings down the weak
that can only exalt
the strong and the brave.

— Gonçalves Dias [1]

---

[1] Gonçalves Dias (1823–1864) was a Brazilian Romantic poet, playwright, ethnographer, lawyer, and linguist. Excerpt reprinted in L. Lúcia Sá, *Rain Forest Literatures: Amazonian Texts and Latin American Culture*, Minneapolis: University of Minnesota Press, 2004.

[*]The Brazilian submarines are named after native-Brazilian colonial tribes as Tupi, Tamoio, Timbira, Tapajó and Tikuna.

THIS PAGE INTENTIONALLY LEFT BLANK

I. INTRODUCTION

Towed sonar arrays are designed for passive and/or active target detection. These arrays are towed by surface ships, submarines, and UUVs (unmanned undersea vehicles). Two important types of towed arrays are a linear array of triplets and a twin-line planar array.

A. MOTIVATION

Towed sonar arrays represent a significant advantage over the sonars installed on the hull of surface ships and submarines, due to their ability to track targets located at longer ranges, reduction of self-noise, and operation at low frequencies (below 1 kHz). According to Urick [1], these frequencies (below 1kHz) usually contain meaningful components of vessel's acoustic signatures, related primarily to machinery noise, like engines, motors, pumps, gears, propeller blades, electrical systems, and appliances. A deeper knowledge of this technology is invaluable for proper acquisition and operation of towed sonar arrays, as well as for developing or improving sonar systems already deployed by the Brazilian fleet. Furthermore, sonar arrays are the basic elements of underwater surveillance networks, planned to be installed along strategic areas of the Brazilian coastline.

B. PROBLEM STATEMENT

There are many reports of improvements on linear arrays of triplets and twin-line planar arrays available in the literature, as summarized in [2], [3], and [4]. Still, the literature lacks a systematic and detailed design approach for these sonars.

The main goal of this research is to evaluate how well a linear array of triplets and a twin-line planar array can solve the port/starboard (PS) ambiguity problem, which occurs when the far-field (FF) beam pattern is symmetric, like in single-line arrays. The symmetry leads to the problem that a target located either at starboard or port side produces the same output signal in the sonar. Figure 1 is the top view of a linear array towed by a submarine while the beam pattern is being steered to search for targets. The

1

steer angle ψ' is measured from the positive X axis to the axis of the mainlobe in the XY plane, hatched in green. At steer angle $\psi' = 45°$, the signal measured in the sonar output indicates the presence of a target, that is, the target is located at bearing angle $\psi_S = 45°$ (starboard side). However, in this example, the target is actually at $\psi_S = 135°$ (port side), which corresponds to the steer angle of the mirror image of the mainlobe in the XY plane. Since both mainlobes have the same magnitude, the array has an identical response for targets located at symmetrical bearing angles, and consequently, the sonar generates the same output, causing the ambiguity.
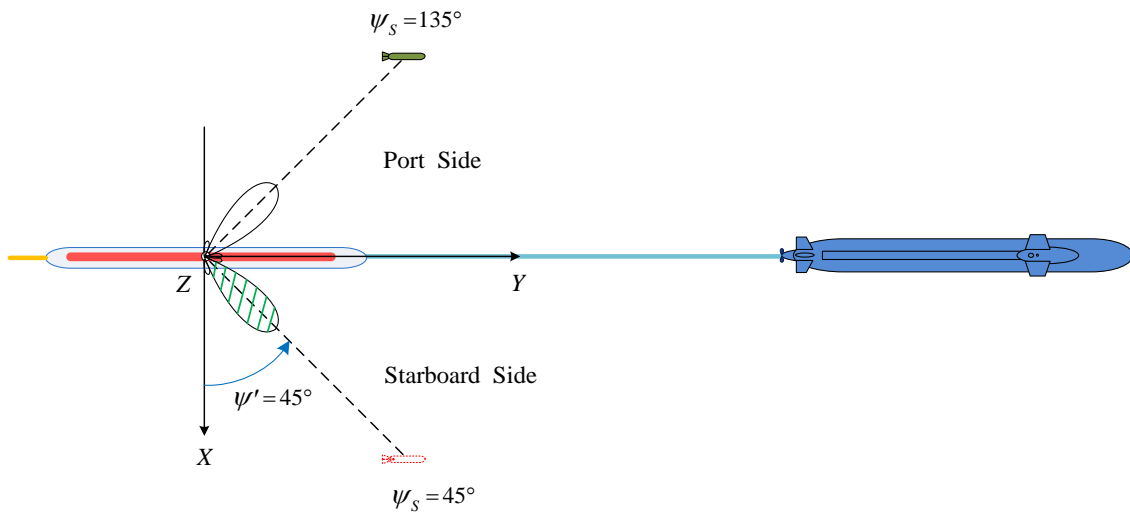
Figure 1   Port/starboard ambiguity problem.

In addition to the PS rejection, the research addresses the following subsidiary questions:

How can these arrays be designed to operate in either the passive or active mode?

What is the relationship between frequency of operation, FF beam patterns, and size?

How sensitive is the horizontal beam pattern of a twin-line planar array to noise?

How well does the FFT (fast Fourier transform) beamforming algorithm perform when processing signal plus noise data?

C. LITERATURE REVIEW

This section presents a general description of towed sonar arrays and their implementations. Initially, the features that may represent an advantage over conventional sonars are examined along with their drawbacks. The basic architecture of a towed sonar array and the characteristics of its components are introduced, as well as the two types of sonars studied—a linear array of triplets and a twin-line planar array. This section concludes with some examples of towed arrays.

1. Background

Towed sonars date back to the "Electric Eel" of WWI, invented in 1917 by the US Navy Physicist H. Hayes. This device was an experimental twin-line array with 12 hydrophones per neutral buoyant cable. Besides the port/starboard ambiguity removal provided by the buoyant arrays, the system was equipped with an additional pair of arrays mounted in the hull of the station towing the twin-line array, meant to allow for passive ranging using both arrays [2]. Since then, pushed by advances on ocean acoustics, electronics, and signal processing, towed sonars have improved drastically. Along with military applications, they have been used for purposes as diverse as oil and gas exploration, geological research, and location of objects on the seafloor.

Towed sonar arrays are not constrained by the length of the vessel's hull like flank sonar arrays in submarines. A longer length enables operation at lower frequencies and yields a higher directivity—which corresponds to an increase in bearing resolution. Nevertheless, the towing of a long cable—up to 2.4 km long at depths up to 360 m in the case of surface ships [4]—brings operational issues. The major problems are the limitation of the vessel's speed, eventual damage by contact with the ocean bottom or fisher nets, setback of sensitive military operations due to time spent on stowage, and limitations on maneuvering.

Another advantage of these arrays is the uncoupling with the vessel's self-noise (machinery noise and cavitation), resulting in a higher SNR and consequent detection and tracking of faint targets. However, this benefit is negated partially by the additional noise introduced by the towed sonar itself. The cabling self-noise due to hydrodynamic forces, in particular the vibrations induced in the towing cable, causes acceleration forces on the sensors [1, p. 372]. The cabling self-noise can be further heightened if the vessel does not keep a straight course or abruptly changes speed during measurements. Some design improvements and mechanical and signal processing compensation techniques have been introduced to overcome or minimize these drawbacks.

Figure 2 shows the basic architecture of towed sonars. The design is based on the "TOWFLEX Principles" established in the early 1960s, as a result of research programs carried out by ONR (Office of Naval Research) and DTMB (David Taylor Model Basin) [4]. The surface ship towing the sonar moves to the right, in the positive *Y* direction. The coordinate system is centered in the middle of the array. This reference frame is utilized throughout this work.

The towed sonar array is essentially composed of three segments: towing cable, flexible hose with the array of acoustic sensors (hydrophones), and stabilization tail.

The following are the fundamental features of the TOWFLEX architecture, as illustrated in Figure 2.

- The towing cable is made long enough to place the array segment below the thermocline. The dotted line illustrates a sound-speed profile $c(z)$, where z is the depth, which takes on negative values below the ocean surface. Hence, the array is put outside the near-field region of the ships' radiated self-noise due to refraction of the travelling sound rays, and at a distance at which this noise is greatly reduced by spreading loss. The directionality provided by the array further reduces the remaining noise coming from the ship [4].

- The flexible hose enclosing the array has a layer filled with oil. The resulting buoyancy improves towing stability and reduces drag. The hose

4

flexibility reduces also resonance characteristic of rigid structures [4], which produces radiated noise, according to [1, p. 333].

- The array is made even more flexible than its enclosing hose, in order to isolate it from cable vibration and also to decouple the array elements from each other. The array is also designed to weaken the acceleration response induced by motion [4].

- The tail with a drogue avoids whip at the end of the array segment [4].

Signal processing techniques further compensate for some of the downsides of towed sonars and also address common problems faced by any sonar. The vertical motion of the vessel introduces errors in the acoustic pressure measured from targets. Moreover, cable twists during navigation cause nonalignment of the array sensors, resulting in errors in the computation of the DOA (direction of arrival). Sensors installed along the cabling measure its pitch and roll, such that they can be compensated for using adaptive techniques [4], [5], and [6]. A statistical average of the sensor's outputs filter out both local noise—ambient sea noise and acoustic pressures in the oil layer from turbulence—as well as element response to mechanical stresses and acceleration forces [4].
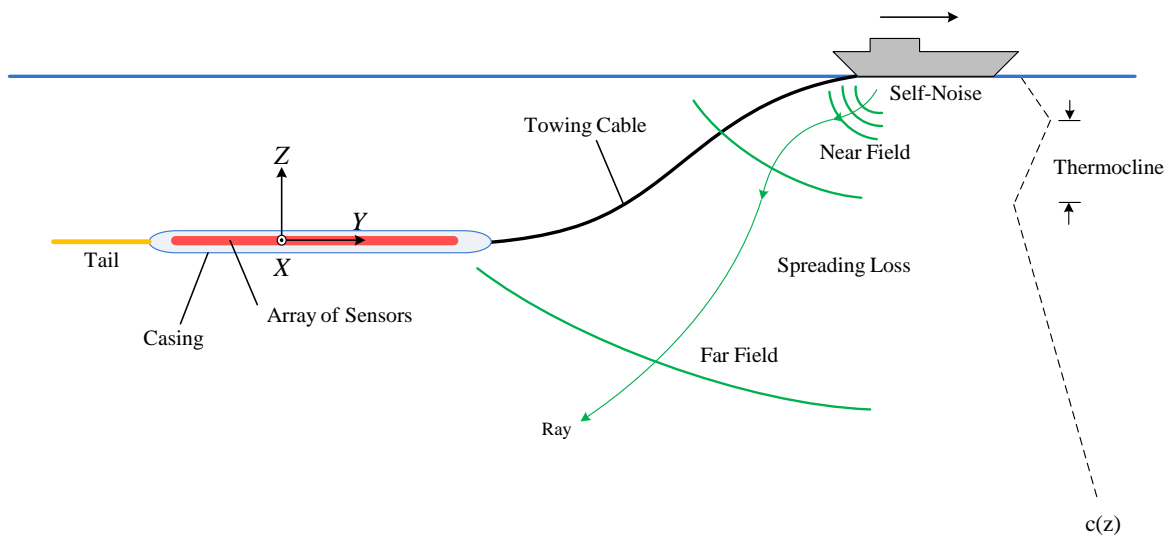
Figure 2   Towed sonar array (adapted from [4]).

The queuing of sensors one after another to build a linear array produces a port/starboard ambiguous FF beam pattern. This issue is solved by special arrangements of sensors in the array, along with proper processing of the received signals, as will be discussed in the next chapters.

The arrangements considered in this work are shown in Figure 3. In Figure 3(a), clusters of single circular arrays composed of three equally-spaced hydrophones, called triplets, are queued to form a linear array. In the second arrangement, shown in Figure 3(b), two linear arrays composed of equally-spaced sensors are combined to yield a twin-line planar array. Regarding the Cartesian coordinate system indicated in these figures, the single triplets lie in the *XZ* plane and are aligned along the *Y* axis, and the twin-line planar array lies in the *XY* plane.

(a)   *(b)*
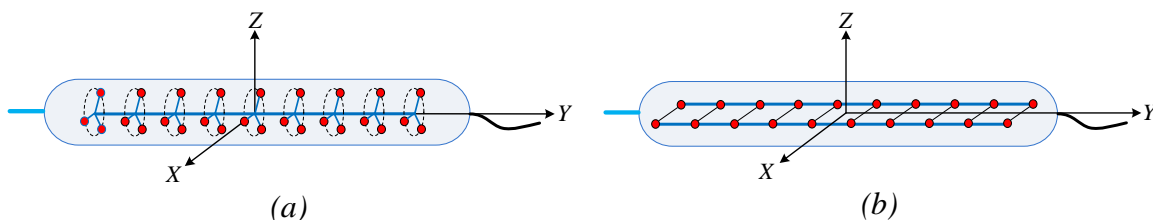
Figure 3   (a) Linear array of triplets, and (b) a twin-line planar array.

2. Implementations

Some implementations of towed sonar arrays are presented below, in order to illustrate actual parameter values, such as array and segment lengths, number of elements, element spacing, and frequency range. The first array [6] exemplifies a hybrid device deploying sensors arranged both as a single-line array and as a linear array of triplets. The following two papers [5] and [7] relate to the same project, a linear array of triplets, used in conjunction with a towed sound source, and address a normalization device and the sonar calibration, respectively. The last paper [8] introduces a new beamforming algorithm for a linear array of triplets.

FORA (Five Octave Research Array) [6] is a mixed towed sonar composed of a linear array of single elements and a linear array of triplets, designed and built by

Chesapeake Sciences Corporation in a joint project with Teledyne, ONR, MIT, and Penn State. The linear array of single elements, which does not provide port/starboard discrimination, has an acoustic aperture of 189 m, and a diameter of 78 mm. The linear array of 78 triplets has an acoustic aperture of 15.6 m and a diameter of 88 mm. The sensors in the single triplet form an equilateral triangle with sides 38.5 mm in length. The linear array of single elements has 256 hydrophones and is divided into four modules for sub-array operation at 250, 500, 1000, and 2000 Hz cutoff frequencies. The cutoff frequency of the linear array of triplets is 3750 Hz. The DAC (digital-to-analog conversion) is performed at the hydrophone channel level (two or four hydrophones per channel) and transmitted through an ATM (Asynchronous Transfer Mode)/SONET (Synchronous Optical Network) network, which is also used for configuration. Additional sensors are distributed along the array for heading, pitch, roll, and depth measurements. The tow cable and the tail drogue are 950 and 305 m long, respectively. The sea trials to assess the several subsystems regarding this project began in 2003 [6].

An example of a linear array composed of triplets alone is presented by NURC (NATO Undersea Research Centre) [5]. This center has developed an LFAS (low frequency active sonar), consisting of a towed sound source and a towed receiver array. The receiver consists of a linear array of triplets and a normalizer. The latter is used to cancel the high background interference caused by reverberation and clutter present in littoral environments. The linear array has 126 triplets. It is divided into two nested sub-arrays, is 35 m long and uses a sampling frequency of 12.8 kHz with LFM (linear frequency modulation) pulses in two frequency bands, 0.8–1.8 kHz and 2–3.62 kHz. Each band is covered by a sub-array with the radii of triplets adjusted for its band's upper limit. NURC's paper [5] describes the steps of signal processing and shows a beam-pattern for a 45° steering direction, with successful PS rejection. Nevertheless, it does not detail the corresponding operating frequency or the complex weights applied. The remaining sections of this paper deal with the performance of the normalization process [5].

Another work of NURC [7] focuses on a linear array of triplets, and addresses two subjects, the calibration of the beamformed output and the compensation of errors

7

due to the twist of the array. According to the authors, calibration is necessary for proper comparison between beam patterns obtained using real and synthetic data, respectively. For this purpose, they derive expressions of calibration factors for CW (continuous wave) and LFM input signals, and analyze the PS rejection for calibrated and non-calibrated data—both real and synthetic. Beamforming expressions are also derived, but the authors do not provide the values of the beamformer's complex weights for PS rejection. Regarding the second subject, the authors derive a hydrophone positioning matrix as a function of the twist angle experienced by each sensor during the towing of the array. Using this matrix and the measurement of the angles through roll sensors along the array, they show how the twist effect can be compensated.

Groen *et al.* [8] propose a novel adaptive triplet beamforming algorithm for LFAS. This algorithm allows the beamformer's complex weights to be adjusted either for PS rejection or for SNR. The first option is appropriate for coastal areas with high directional reverberation, while the second option is more suitable for deep water, where the major concern is omnidirectional noise.

D.   METHODOLOGY AND THESIS ORGANIZATION

This research is limited to mathematical modeling and computer simulations. The mathematical models for a single triplet, a linear array of triplets, and a twin-line planar array are implemented in Matlab. The behavior of their FF beam patterns as a function of frequency is studied. A comparative investigation on the performance of these arrays to solve the PS ambiguity problem is then carried out. Nevertheless, for further analyses, the research is focused only on the twin-line planar array.

A signal generator is coded in Matlab, based on a theoretical model and designed specifically to simulate the signals reaching the sensors of a twin-line planar array. The sound-source radiates a rectangular-envelope CW pulse, and is positioned in the FF region of the array. The received signal is beamformed, and the measured bearing angle is compared to the known bearing angle set for the source. After assessed in a no noise situation, the performance of the array is tested in the presence of noise and their effects are evaluated.

Backed by these results and analyses, one is able to evaluate the efficacy of the simulated twin-line planar array, and then summarize the characteristics of the simulation, its advantages, constraints and operational conditions for best performance.

Chapter II introduces the single triplet and examines its ability to resolve the PS ambiguity, and Chapter III extends this study for a set of triplets combined as a linear array of triplets. The remaining chapters are devoted to the twin-line planar array. Chapter IV describes the twin-line planar array, investigates its PS rejection capability, and presents a method for configuring sub-arrays. Chapter V describes the signal processing performed in the array and introduces a simulation tool for assessing its performance—a signal generator. Additionally, Chapter V details the implementation of beamforming using forward and inverse DFTs, and presents a method of computing beam patterns utilizing a two-dimensional spatial DFT. Chapter VI assesses the ability of the twin-line planar array to determine the location of a simulated target in the presence of noise. Chapter VII summarizes the thesis research and presents recommendations.

THIS PAGE INTENTIONALLY LEFT BLANK

II. ANALYSIS OF A SINGLE TRIPLET

This chapter presents a study of the FF (far-field) beam pattern of a single triplet. The first section introduces the single triplet, with its definition, and the second section discusses the theoretical expression of the associated beam pattern. Some examples illustrate how the complex weights modify the shape of the beam pattern, and, more specifically, which complex weights yield a cardioid-shaped FF beam pattern, in order to eliminate the PS (port/starboard) ambiguity. An investigation of the dependence of the beam pattern on frequency allows one to determine the frequency constraints for keeping the cardioid shape. Based on this analysis, a method of beam pattern equalization is proposed. The derivation of an expression for the radial extent of a triplet as a function of frequency, as well as a discussion of the operational impact regarding this radius, concludes the study.

A. SINGLE TRIPLET

A single triplet is a circular planar array composed of three identical, equally-spaced, omnidirectional point-elements. This circular array can be positioned in the *XZ* plane, so that the horizontal beam pattern lies in the *XY* plane, and the vertical beam pattern lies in the *XZ* plane, according to the right-handed Cartesian coordinate system of Figure 4(a). Adopting the positive *Y* axis as the direction of towing the triplet, as deployed in towed sonar arrays, the positive *X* axis will correspond to the starboard side, and the negative *X* axis to the port side.

The rectangular coordinates (x_n, z_n) of the nth point-element in the array are defined in terms of the angle ϕ_n between the *X* axis and the polar radius a at the position of the element, and are given by

$$x_n = a \cos \phi_n \tag{2.1}$$

$$z_n = a \sin \phi_n \tag{2.2}$$

where n is equal to 1, 2 or 3, and ϕ_n, in radians, is given by

$$\phi_n = (n-1)\, 2\pi/3. \tag{2.3}$$

The rectangular coordinates for element 2 in the triplet are illustrated in Figure 4(b).
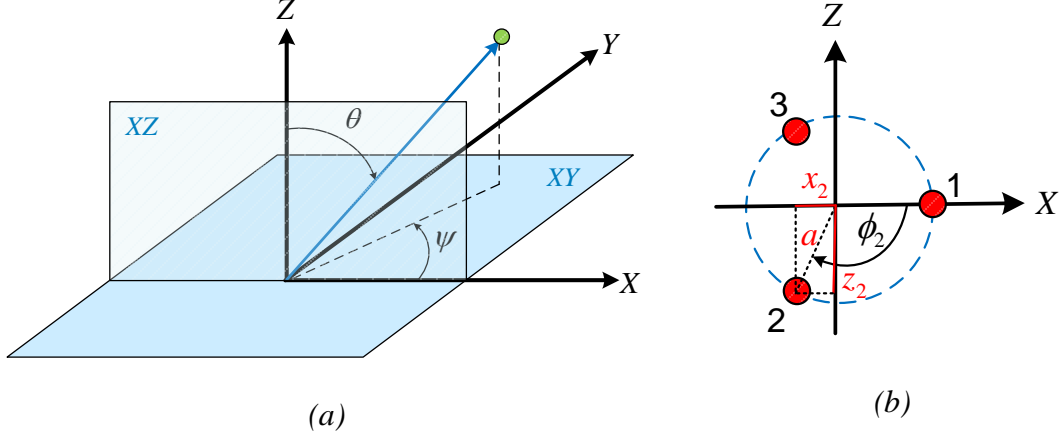
Figure 4   (a) Right-handed Cartesian coordinate system, and (b) a single triplet in the *XZ* plane.

B.   FAR-FIELD BEAM PATTERNS

The unnormalized, far-field beam pattern, $D(f,u,w)$, of a single triplet with radial extent a and lying in the *XZ* plane is given by the following expression [9, where direction cosine v is replaced with direction cosine w in Example 8.1-7]

$$D(f,u,w) = \mathbb{S}(f)\sum_{n=1}^{3} c_n(f)\, e^{jk(ux_n + wz_n)} \tag{2.4}$$

where

$$u = \sin\theta\, \cos\psi \tag{2.5}$$

and

$$w = \cos\theta \tag{2.6}$$

are dimensionless direction cosines with respect to the *X* and *Z* axes, respectively, defined in terms of the spherical angles θ and ψ,

$$k = 2\pi/\lambda \tag{2.7}$$

is the wavenumber corresponding to wavelength λ and frequency f, x_n and z_n are the rectangular coordinates of the nth triplet element, $\mathbb{S}(f)$ is the element sensitivity function, and $c_n(f)$ is the complex weight used for the nth element.

The complex weight $c_n(f)$ has amplitude $a_n(f)$ and phase $\varphi_n(f)$, which can be written in terms of the product of the wavenumber k, the radial extent of the single triplet a, and a constant C_n, as shown below:

$$c_n(f) = a_n(f)\, e^{j\,\varphi_n(f)} = a_n(f)\, e^{j\,C_n ka}. \tag{2.8}$$

Both the amplitude $a_n(f)$ and the phase $\varphi_n(f)$ can be adjusted to conveniently modify the shape of the beam pattern of the single triplet, as demonstrated in the following examples.

1. Far-Field Beam Patterns with no Phase Weights

The far-field beam patterns of Figure 5 were obtained by setting the operating frequency at 1000 Hz, and applying the following rectangular amplitude weights

$$a_1(f) = 2 \tag{2.9}$$

$$a_2(f) = a_3(f) = 1 \tag{2.10}$$

and phase weights $\varphi_n(f)$ equal to zero in Equation (2.8).

Figure 5(a) shows the unnormalized, horizontal FF beam pattern in the XY plane, obtained from Equation (2.4) by setting $\theta = 90°$. Figure 5(b) shows the unnormalized, vertical FF beam pattern in the XZ plane, obtained from Equation (2.4) by setting $\psi = 0°$ (positive X axis) and $\psi = 180°$ (negative X axis). Port/Starboard (PS) ambiguity occurs in both beam patterns. The first one has maxima at $0°$ and $\pm 180°$ [Figure 5(a)], and the second one at $-90°$ and $+90°$ [Figure5 (b)].

(a)   *(b)*
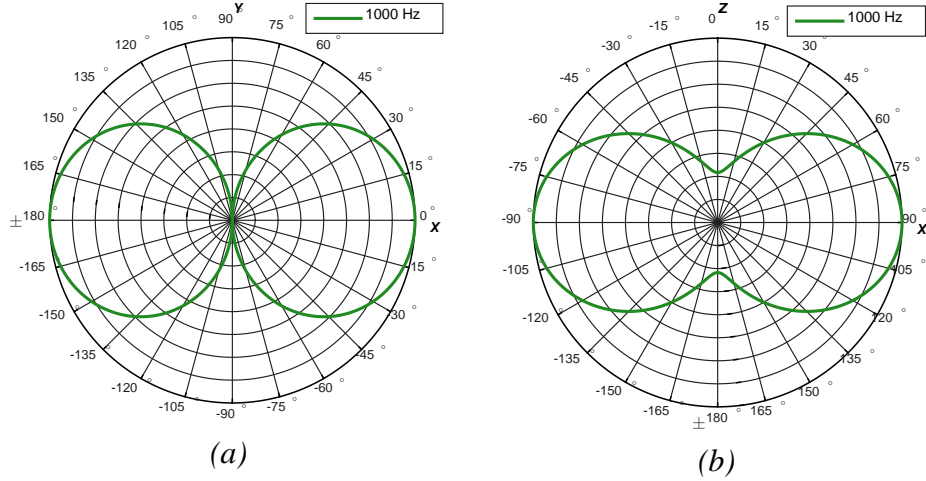
Figure 5   (a) Unnormalized, horizontal FF beam pattern in the *XY* plane with no phase weights as a function of bearing angle ψ, and (b) unnormalized, vertical FF beam pattern in the *XZ* plane with no phase weights as a function of vertical angle θ.

2.   Far-Field Beam Patterns with Phase Weights

The PS ambiguity observed in Figure 5 can be rejected by changing the complex weights to the following values [9]:

$$c_1(f) = -2a(f)e^{jC_1 ka} = -2a(f)e^{j\frac{3}{2}\frac{\pi}{3}} = -2a(f)e^{j\frac{\pi}{2}} = 2a(f)e^{-j\frac{\pi}{2}} \tag{2.11}$$

$$c_2(f) = c_3(f) = a(f) \tag{2.12}$$

where $C_1 = 3/2$ and $ka = \pi/3$ in $c_1(f)$, $C_2 = C_3 = 0$ in $c_2(f)$ and $c_3(f)$, and $a(f) = 1$ [see Equation (2.8)].

These complex weights lead to the cardioid-shaped, unnormalized beam patterns shown in Figure 6(a) for the horizontal FF beam pattern in the *XY* plane, and Figure 6(b) for the vertical FF beam pattern in the *XZ* plane. In both beam patterns the ambiguous mainlobe at portside was suppressed. The beam patterns can be steered to the port side by using a positive $\pi/2$ phase weight in $c_1(f)$ [9], as shown in Figure 7(a) for the unnormalized, horizontal FF beam pattern in the *XY* plane, and Figure 7(b) for the unnormalized, vertical FF beam pattern in the *XZ* plane.

14
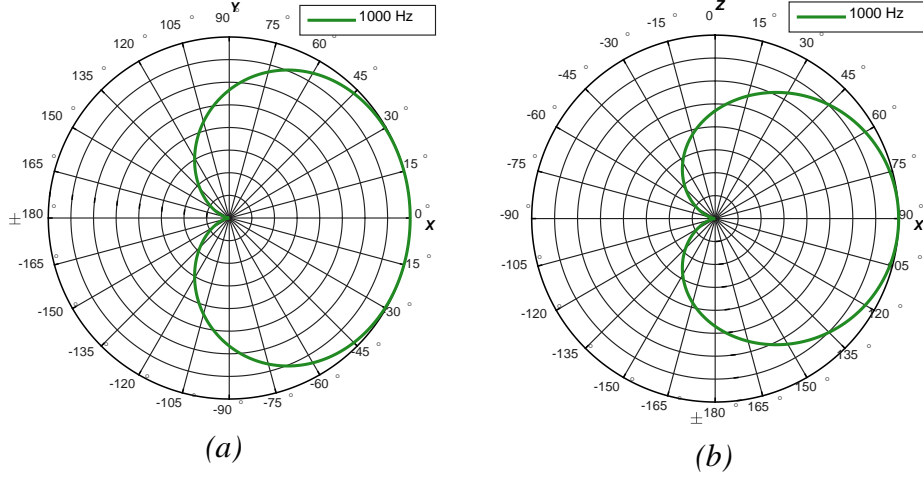
Figure 6   (a) Unnormalized, horizontal FF beam pattern in the *XY* plane
steered to starboard side, and (b) unnormalized, vertical FF beam pattern
in the *XZ* plane steered to starboard side.
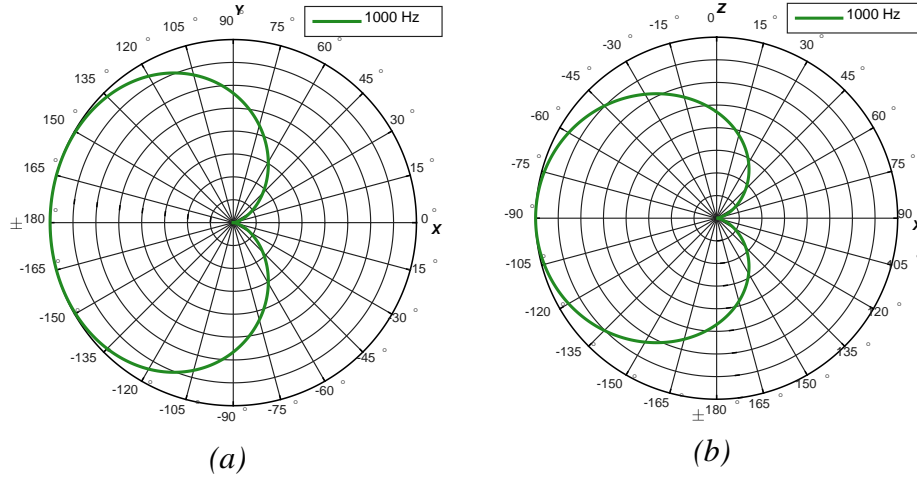
Figure 7   (a) Unnormalized, horizontal FF beam pattern in the *XY* plane
steered to port side, and (b) unnormalized, vertical FF beam pattern in
the *XZ* plane steered to port side.

3.   Beam Pattern vs. Frequency

This section examines the behavior of the FF beam pattern of a single triplet as
the frequency is varied. Denoting f_a as the frequency that corresponds to $k_a a = \pi/3$ ($\pi/3$

15

is the value used for ka in Equation (2.11) to obtain the cardioid beam pattern) one can derive an expression for ka as a function of f_a, as follows:

$$k_a a = \frac{\pi}{3} \quad \rightarrow \quad \frac{2\pi f_a}{c}a = \frac{\pi}{3} \quad \rightarrow \quad a = \frac{c}{6 f_a} \tag{2.13}$$

$$ka = \frac{2\pi f}{c}a \quad \rightarrow \quad ka = \frac{2\pi f}{c}\frac{c}{6 f_a} \quad \rightarrow \quad ka = \frac{\pi}{3}\frac{f}{f_a}. \tag{2.14}$$

One can note that when frequency f is set equal to f_a in Equation (2.14), then the product ka is equal to $\pi/3$. Thus, for the study of the FF beam pattern as a function of frequency, one can start with a value for frequency f_a in the required range of operation. Then, using Equation (2.13), the radial extent a of the triplet can be computed. Next, one can take a frequency range around f_a in order to examine the behavior of the shape of the beam pattern when ka gets lower or higher than the optimum value $\pi/3$. The expression for the unnormalized, FF beam pattern used in this study was obtained by substituting Equation (2.14) into Equation (2.4) yielding

$$D(f,u,w) = \mathbb{S}(f)\sum_{n=1}^{3}c_n(f)e^{jk(ux_n + wz_n)} = \mathbb{S}(f)\sum_{n=1}^{3}c_n(f)e^{jka\left(u\frac{x_n}{a}+w\frac{z_n}{a}\right)} \tag{2.15}$$

$$D(f,u,w) = \mathbb{S}(f)\sum_{n=1}^{3}c_n(f)e^{j\frac{\pi}{3}\frac{f}{f_a}\left(u\frac{x_n}{a}+w\frac{z_n}{a}\right)}. \tag{2.16}$$

In this study, frequency f_a was set to 1000 Hz, which, as discussed in Chapter I, is the upper limit of a range of significant acoustical frequency components. This frequency corresponds to a single triplet with a radius of 250 mm. The unnormalized, horizontal FF beam pattern in the *XY* plane was plotted for a frequency range between 10 Hz and 1700 Hz, subdivided in intervals, as shown in Figure 8. For the sake of comparison, frequency f_a is included in all of the intervals.
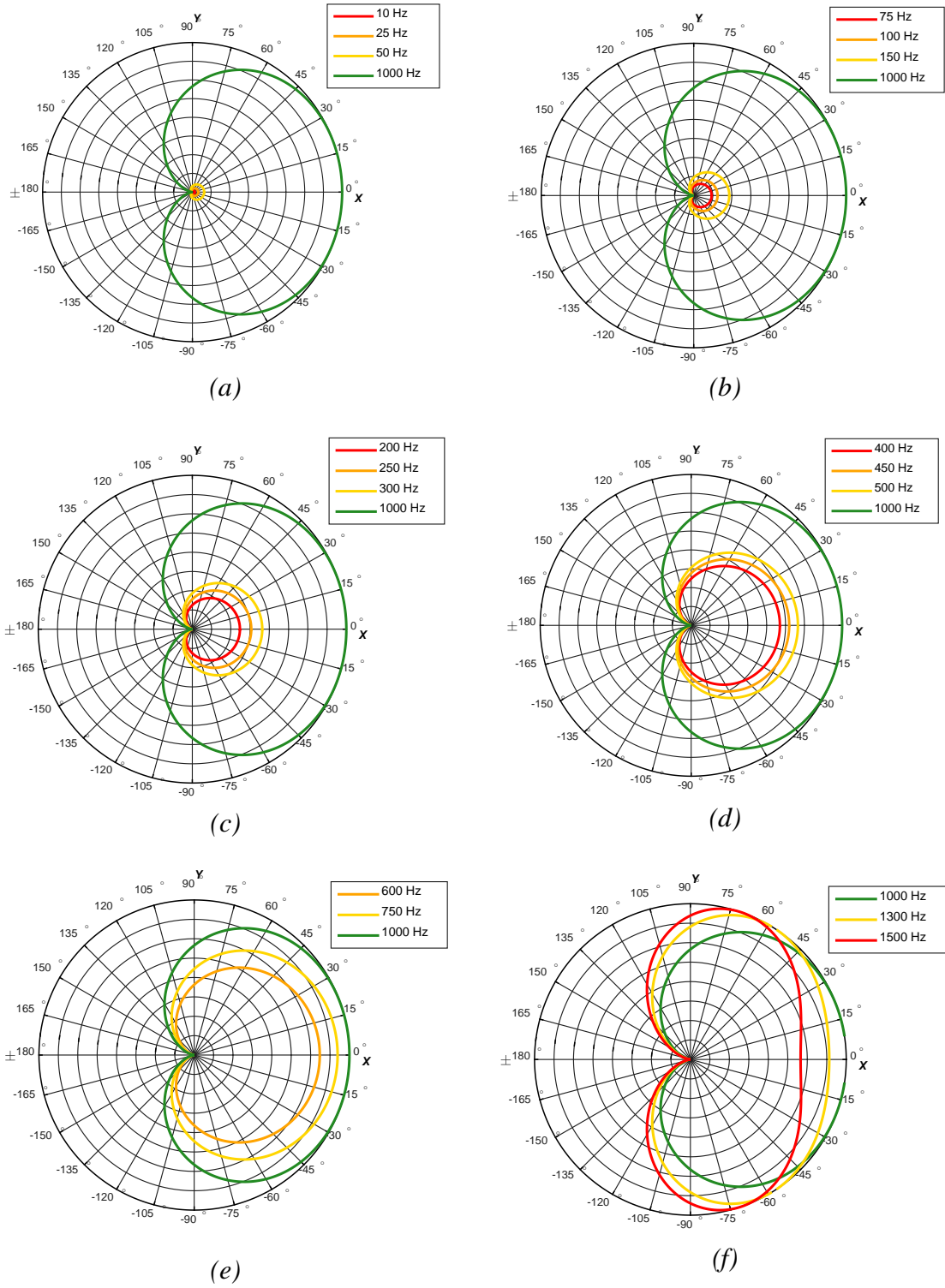
Figure 8   Unnormalized, horizontal FF beam patterns in the *XY* plane vs. bearing angle ψ and frequency.

(g)
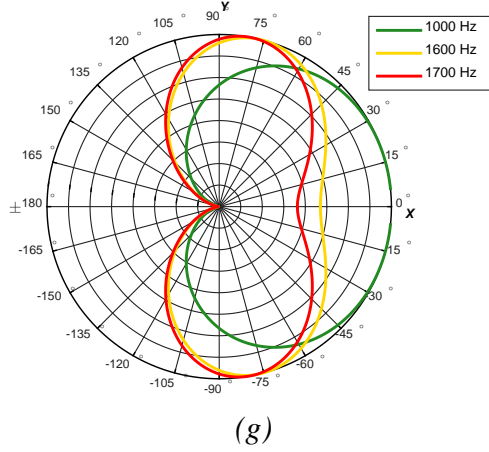
Figure 8. (Continued.)

For frequencies below f_a, the beam patterns kept the cardioid shape—even for values far lower than f_a—but the magnitude decreased in comparison to the beam pattern corresponding to $f = f_a$. However, for frequencies well above f_a, the cardioid started to turn into a distorted dipole. This dipole is rotated $\pi/2$ rad relative to the case seen before, when no phase weights were applied (see Figure 5). The same behavior was observed for unnormalized, vertical FF beam patterns in the *XZ* plane. This distortion can be understood by examining the expressions for the beam pattern and the complex weight $c_1(f)$ as follows.

Substituting Equation (2.11) into the first term of the summation in Equation (2.16) yields

$$c_1(f)e^{j\frac{\pi}{3}\frac{f}{f_a}\left(u\frac{x_1}{a}+w\frac{z_1}{a}\right)} = 2a(f)e^{-j\frac{\pi}{2}}e^{j\frac{\pi}{3}\frac{f}{f_a}\left(u\frac{x_1}{a}+w\frac{z_1}{a}\right)} = 2a(f)\ e^{j\left[\frac{\pi}{3}\frac{f}{f_a}\left(u\frac{x_1}{a}+w\frac{z_1}{a}\right)-\frac{\pi}{2}\right]}. \qquad (2.17)$$

For f greater than f_a, the first term in the exponent becomes more dominant over the second term, which is the phase weight $-\pi/2$. Therefore,

$$2a(f)\ e^{j\left[\frac{\pi}{3}\frac{f}{f_a}(u\frac{x_1}{a}+w\frac{z_1}{a})-\frac{\pi}{2}\right]} \simeq 2a(f)e^{j\frac{\pi}{3}\frac{f}{f_a}\left(u\frac{x_1}{a}+w\frac{z_1}{a}\right)} \qquad (2.18)$$

18

and the beam pattern starts losing its cardioid shape and approaches a dipole shape as observed in Figure 8(g).

However, for f less than f_a, the phase weight $-\pi/2$ in the exponent of Equation (2.17) becomes more dominant over the first term, and the cardioid shape is kept. However, the lower the ratio f/f_a, the lower the magnitude of the first term in the exponent, which leads to progressive shrinking of the cardioid, as seen in Figure 8(f) and (g). Nevertheless, the decrease in magnitude of the beam pattern for frequencies below f_a can be compensated for by the equalization of their beam patterns, using as a reference the maximum magnitude, D_{MAX}, given by

$$D_{MAX} = |D(f_a, 90°, 0°)|. \tag{2.19}$$

The equalized version of an unnormalized, horizontal FF beam pattern in the XY plane $D(f, 90°, \psi)$ can be obtained by using the following expression:

$$D(f, 90°, \psi)_{eq} = \frac{D_{MAX}}{\max |D(f, 90°, \psi)|} D(f, 90°, \psi) = \frac{|D(f_a, 90°, 0°)|}{\max |D(f, 90°, \psi)|} D(f, 90°, \psi). \tag{2.20}$$

Figure 9 shows how the equalization effectively compensates for the decrease in magnitude observed in the previous beam patterns.

(a)   (b)
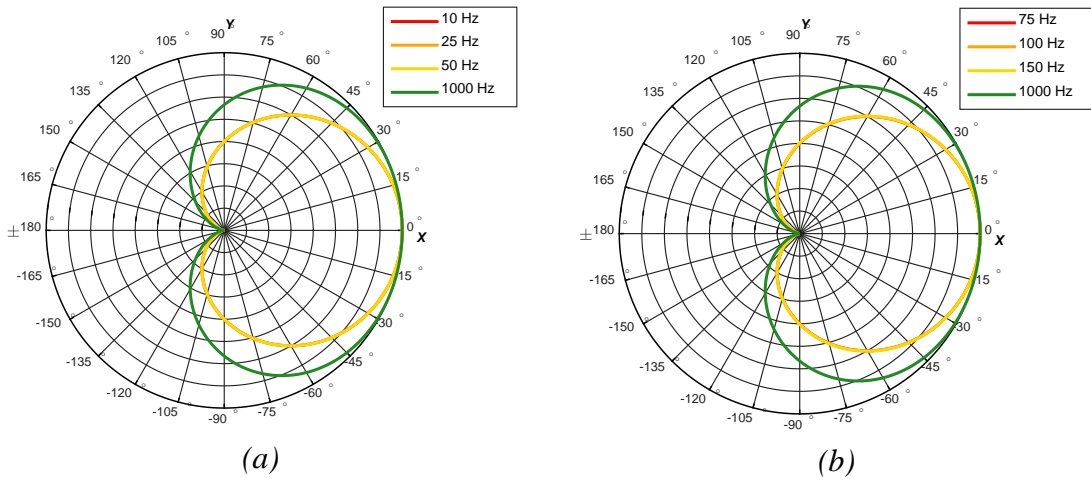
Figure 9   Equalized, horizontal FF beam patterns in the *XY* plane vs. bearing
angle ψ and frequency.

19
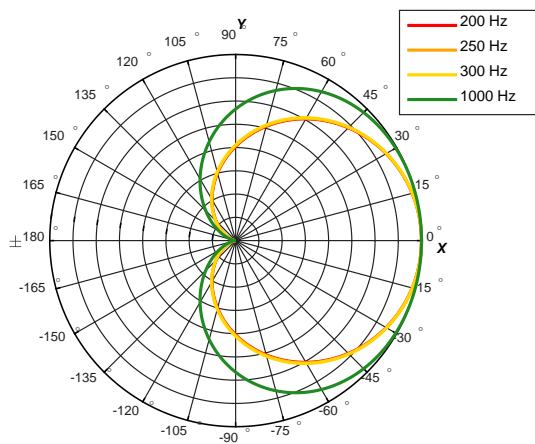
(c)
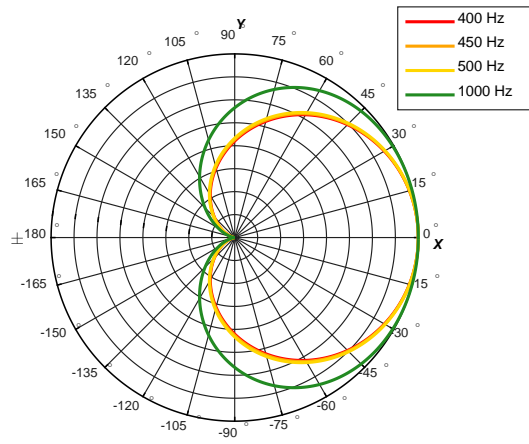
(d)
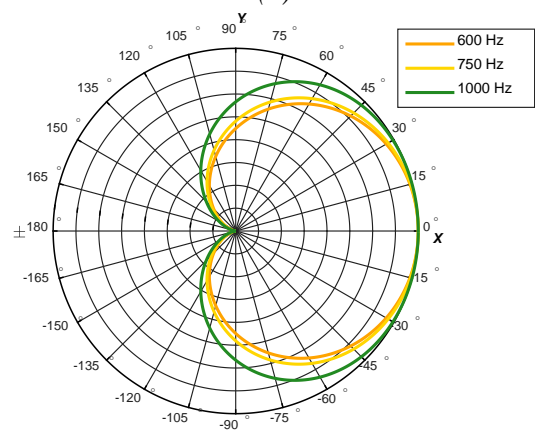
(e)
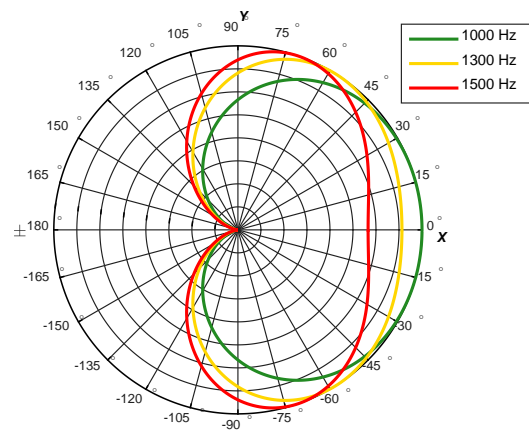
(f)
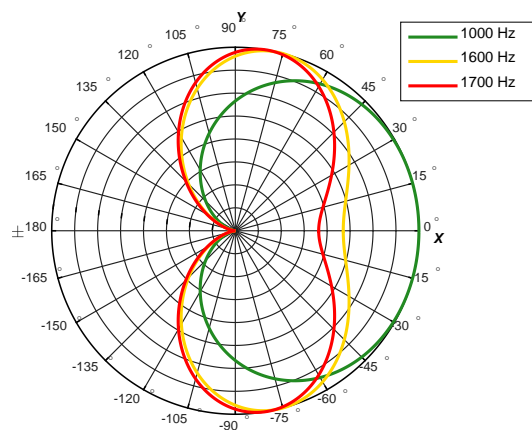
(g)

Figure 9. (Continued.)

20

4.   Radius of the Triplet

As was previously discussed, the acoustic signature of a target determines the frequency f_a, which, in turn, determines the radius of the triplet. Recalling the discussion in Chapter I on the operational drawbacks of towed sonar arrays, the difficulty of deploying and stowing a long cable increases with its diameter. The cable weight and volume increase with the radius a requires a greater power to tow and withdraw the sonar array. In addition, the towed array occupies a larger area in the already restricted loading space of a submarine.

The radius of a triplet for a set of frequencies f_a is listed in Table 1, using Equation (2.13)

Table 1   Radius of the single triplet vs. frequency.

Frequency (f_a) (Hz)	Radius (a) (m)
10	25
50	5
250	1
500	0.5
1000	0.25

From the results obtained for the equalized beam patterns in the previous section, one can conclude that by setting the radius a of the triplet to 0.25 m, the maximum magnitudes of the beam patterns at $\psi = 0°$ for frequencies as low as 10 Hz is the same as that obtained for 1000 Hz, with no distortion of the cardioid shape. Therefore, the triplet can be designed such that, for a required frequency range, the maximum frequency is used to set the diameter of the triplet. In addition, equalization will nearly guarantee uniformity of the beam patterns over this frequency range. As an example, for the upper limit of 1 kHz, the required triplet diameter would be 0.5 m.

The single triplet is the building block of the array to be presented in the next chapter. The comprehensive knowledge acquired so far is valuable to understand the role

of an individual triplet in the behavior of a linear array of triplets. The behavior of the array depends not only on the physical arrangement of the triplets, but also on their beam patterns as a function of frequency.

III.   LINEAR ARRAY OF TRIPLETS

This chapter examines the behavior of a set of single triplets combined as a linear array. The analysis consists of evaluating the effects of frequency variation and beam steering on the FF (far-field) beam pattern of the linear array. These results can be used as a reference to set the operation boundaries of the sonar array.

A.   LINEAR ARRAY

Figure 10 shows a linear array of an odd number $N = 5$ of identical triplets lying along the Y axis. The triplets lie in the XZ plane and are equally spaced, separated from each other by a distance d_Y.
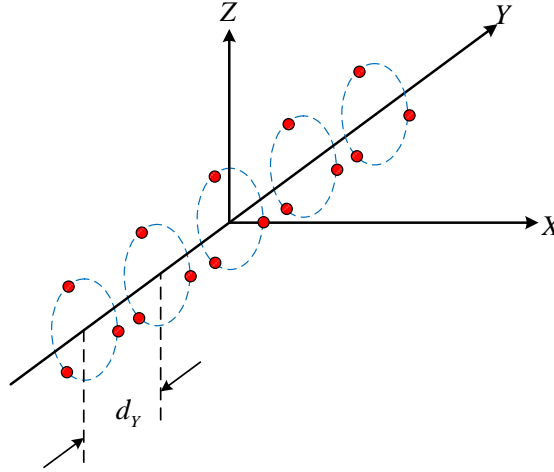
Figure 10   Linear array of triplets.

In order to avoid grating lobes for all possible directions of beam steering, the inter-element spacing d_Y must be less than half the wavelength λ corresponding to the frequency of operation. Given a range of frequencies specified for the linear array of triplets, the following limit for the ratio d_Y / λ must be taken into account in the design of the array [9, Subsec. 6.5.1].

$$d_Y < \frac{\lambda_{min}}{2} \tag{3.1}$$

23

$$d_Y < \frac{c}{2 f_{\max}} \;\rightarrow\; \frac{d_Y}{\lambda} < \frac{c}{2\lambda f_{\max}} = \frac{c}{2(c/f) f_{\max}} \;\rightarrow\; \frac{d_Y}{\lambda} < \frac{f}{2 f_{\max}} \tag{3.2}$$

where $f_{\max}$ is the upper limit of the specified frequency range. The ratio d_Y / λ is one of the parameters in the expression of the beam pattern of the array.

B. FAR-FIELD BEAM PATTERNS

According to the Product Theorem, the unnormalized, FF beam pattern of a linear array of N identical triplets is given by [9, Ch. 9, Example 9.1-2]

$$D(f,u,v,w) = E(f,u,w)\; S_Y(f,v) \tag{3.3}$$

where $E(f,u,w)$ is the unnormalized, FF beam pattern of an individual triplet in the XZ plane, given by Equation (2.4) and here denoted as the beam pattern of a single element, and $S_Y(f,v)$ is the dimensionless array factor in the Y direction given by [9, Ch. 9, Example 9.1-2]

$$S_Y(f,v) = \sum_{n=-N'}^{N'} w_n(f) e^{\,j\,2\pi\, v\, n\, \frac{d_Y}{\lambda}} \tag{3.4}$$

$$N' = (N-1)/2 \tag{3.5}$$

and $w_n(f)$ is the complex weight applied to element n.

The array factor is the response of the array as a function of direction and frequency due to the spatial arrangement of its elements, and the complex weights applied. Complex weights allow modifying the contribution of each element in the array, both in amplitude and in phase, in order to change the overall response, and steer the beam pattern to a required direction, as if the array itself were rotated to this direction.

The complex weight $w_n(f)$ is given by [9, Ch. 9, Example 9.1-2]

$$w_n(f) = b_n(f) e^{\,-j\,2\pi\, v'n\, \frac{d_Y}{\lambda}} \tag{3.6}$$

where $b_n(f)$ is a real, frequency-dependent, dimensionless amplitude weight, and

$$v' = \sin\theta' \sin\psi' \tag{3.7}$$

where θ' and ψ' are the beam-steer angles. Substituting Equation (3.6) into Equation (3.4), using rectangular amplitude weights for $b_n(f)$, and adopting the upper limit for the ratio d_Y / λ given by Equation (3.2), the array factor can be rewritten as

$$S_Y(f,v) = \sum_{n=-N'}^{N'} e^{-j\,2\pi\,(v'-v)n\frac{d_Y}{\lambda}} = \sum_{n=-N'}^{N'} e^{-j\,2\pi\,(v'-v)n\frac{f}{2f_{max}}}. \tag{3.8}$$

The analysis presented in this chapter is based on the equalized, FF horizontal beam patterns in the *XY* plane, which were calculated for an array of 11 triplets lying along the *Y* axis using Equation (2.4) for $E(f,u,w)$, and Equations (3.3) and (3.8). For a horizontal beam pattern in the *XY* plane, one sets $\theta = 90°$ and $\theta' = 90°$. The sets of equalized beam patterns in the *XY* plane for the single triplet obtained in Chapter II were used for $E(f,u,w)$ in the calculation of $D(f,u,w)$, and the frequency f_{max} in Equation (3.8) was set equal to $f_a = 1000$ Hz.

The first set of FF beam patterns, shown in Figure 11, was calculated with no beam steering, that is, with the phase weights set to zero. The same equalization method used for the single triplet, defined by Equation (2.20), was applied here. These results show that using just 11 triplets in a linear array leads to beam patterns with a sharp mainlobe for the frequency interval 600–1000 Hz (f_a), which translates into a higher directivity relative to the original single triplet beam pattern.
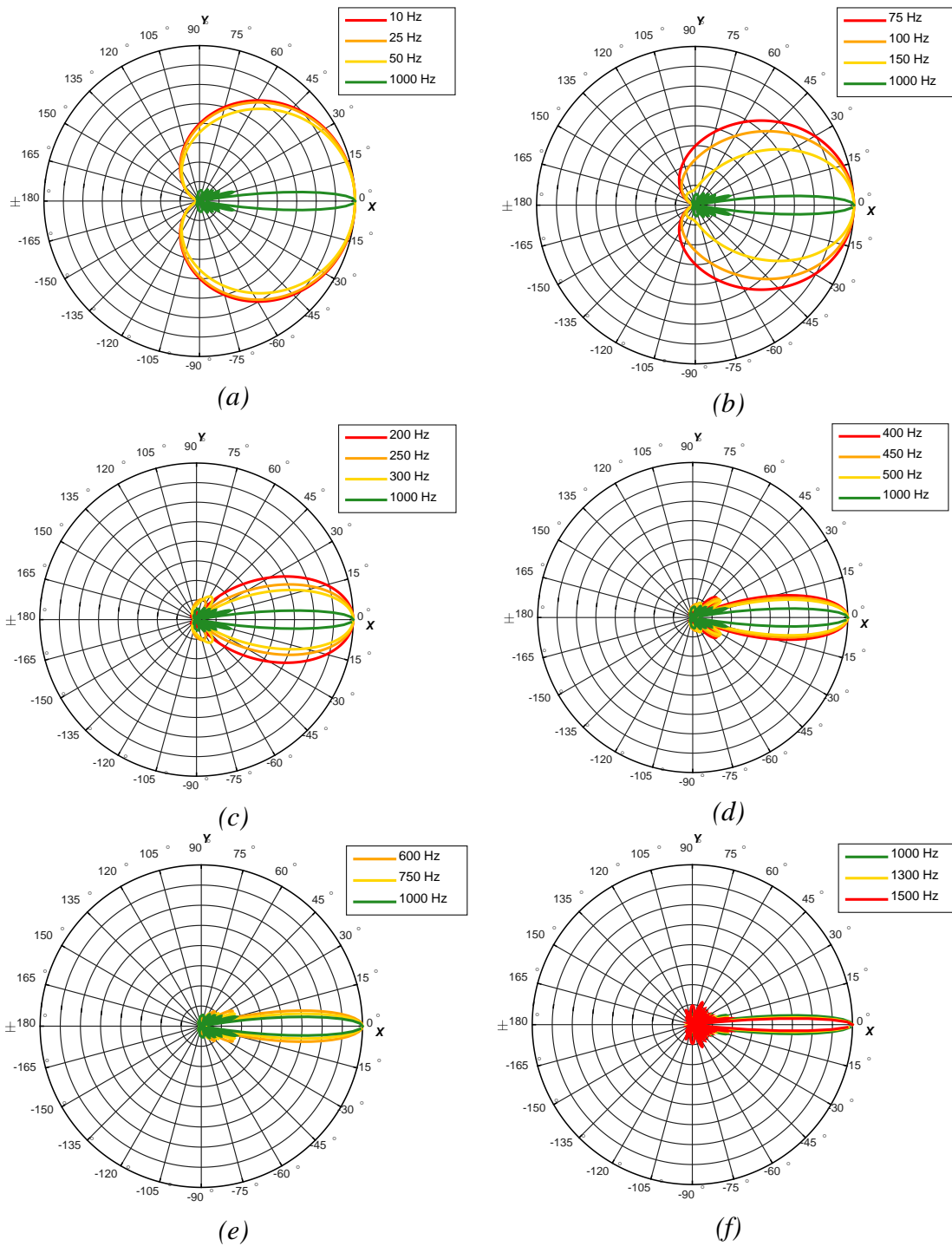
Figure 11   Equalized, horizontal FF beam patterns in the *XY* plane of a linear array of 11 triplets vs. frequency and bearing angle ψ, with no beam steering.

26

(g)
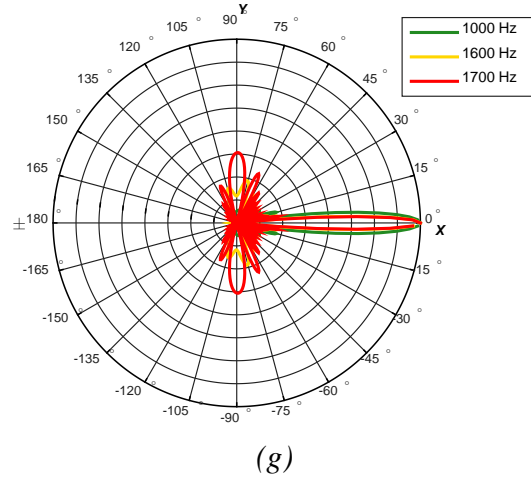
Figure 11. (Continued.)

However, for frequencies below 100 Hz—the region where the single triplet was so well-behaved—using triplets in a linear array has no effect on the FF beam patterns. This performance can be understood by examining the linear plot of the beam pattern. One can notice in the linear plots shown in Figure 12 the increase in the width of the mainlobe with a decrease in frequency, with the consequent reduction of array directivity (bearing resolution). This is the expected behavior for a fixed-size aperture, when the operating frequency is decreased [9, Sec. 2.2]. Despite the loss in bearing resolution—which could be compensated for by increasing the number of elements in the array—the operation at lower frequencies still avoids PS ambiguity. Regarding grating lobes, which are expected to arise at frequencies above f_a, one can observe in Figure 11(f) and (g), that with no beam steering, there is a margin of operation free of grating lobes, which extends up to 1700 Hz, where large sidelobes start to appear.
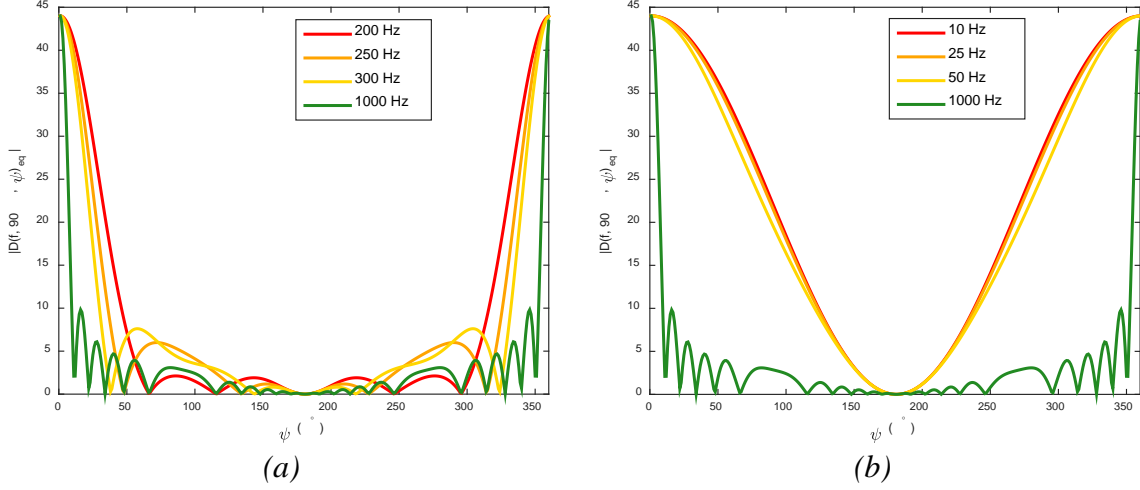
Figure 12   Equalized, horizontal FF beam patterns in the *XY* plane of a linear array of 11 triplets vs. frequency and bearing angle ψ, with no beam steering.

The series of equalized, FF horizontal beam patterns shown in Figure 13 to Figure 16 is a study of the effect of beam steering on the original beam patterns previously shown in Figure 11. The first series refers to 15° beam steering and is shown in Figure 13. A large sidelobe appears at 1500 Hz. For the very low frequencies between 10 and 50 Hz, the beam patterns apparently did not undergo steering at all, but the maxima between -15° and 15° are virtually the same.
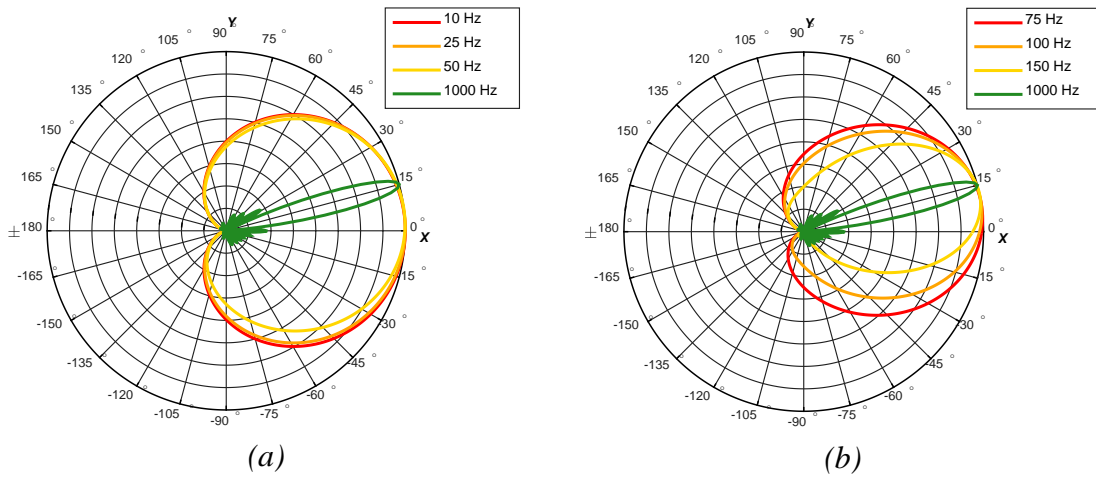
Figure 13   Equalized, horizontal FF beam patterns in the *XY* plane of a linear array of 11 triplets vs. frequency and bearing angle ψ, steered to 15°.

28
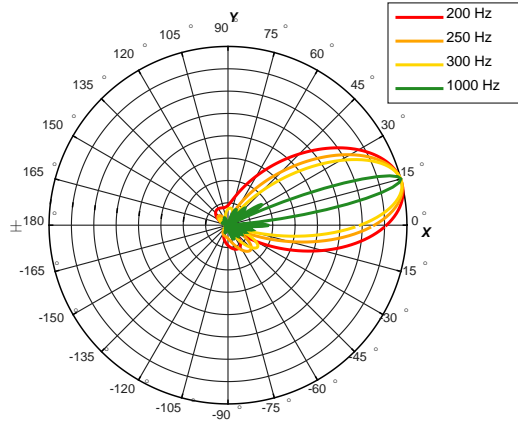
(c)
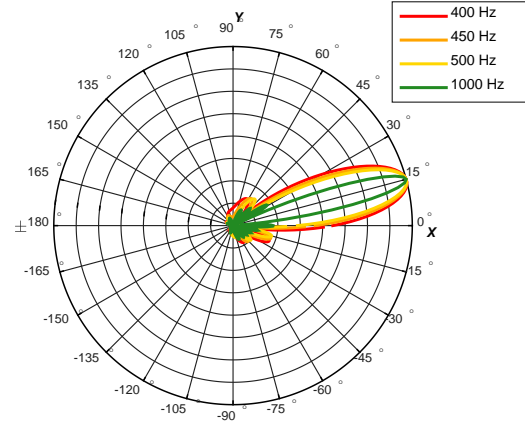
(d)
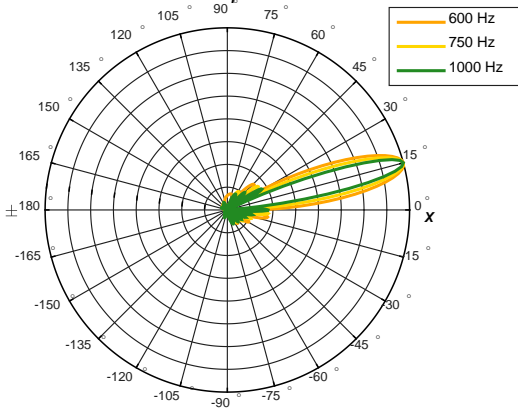
(e)
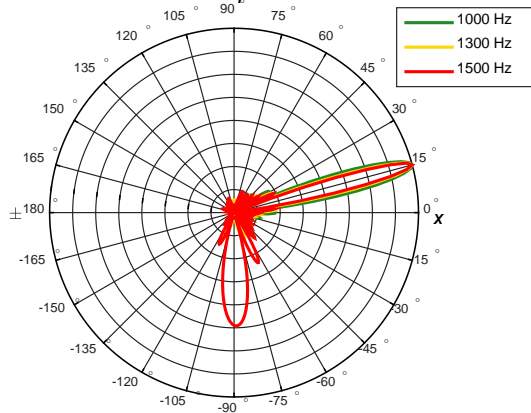
(f)

Figure 13. (Continued.)

The absence of beam steering for low frequencies is more noticeable in the second series, shown in Figure 14, where the mainlobe maxima matches the 30° steer angle only in the interval of 500–1000 Hz. Above 1000 Hz, the beam pattern shows significant sidelobes.
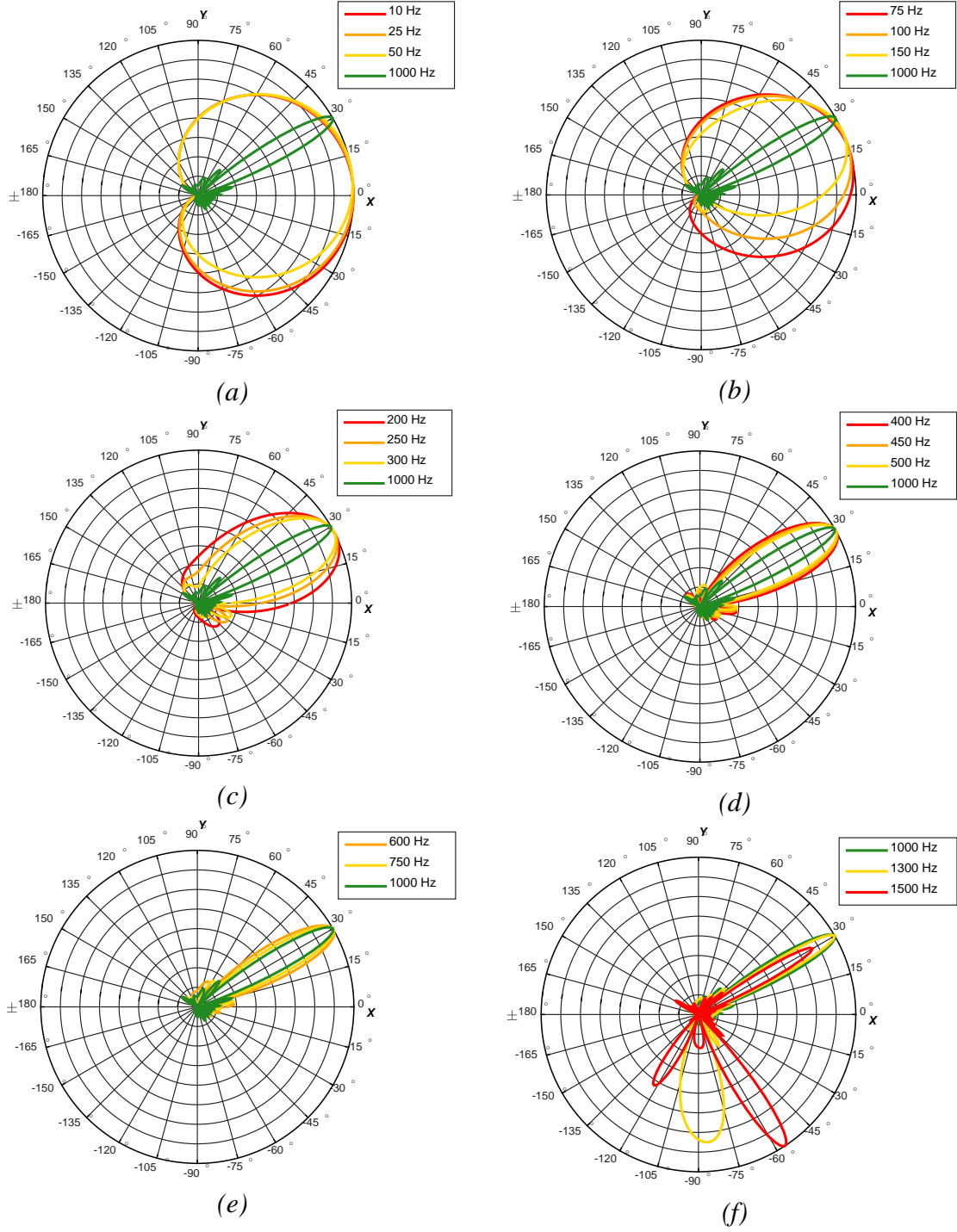
Figure 14   Equalized, horizontal FF beam patterns in the XY plane of a linear
array of 11 triplets vs. frequency and bearing angle ψ , steered to 30°.

The increase of beam steering to 45° further reduces the interval of operation to 600–1000 Hz, as shown in Figure 15. Below 600 Hz, the beam patterns are distorted and not properly steered to 45°. Even the beam pattern corresponding to 1000 Hz (f_a) shows higher sidelobes. As the beam pattern is steered from broadside towards end-fire, the mainlobe becomes asymmetrical and the 3-dB beamwidth increases [9, Sec. 2.5]. The smallest value for the 3-dB beamwidth of the mainlobe is at broadside [9, Sec. 2.5].
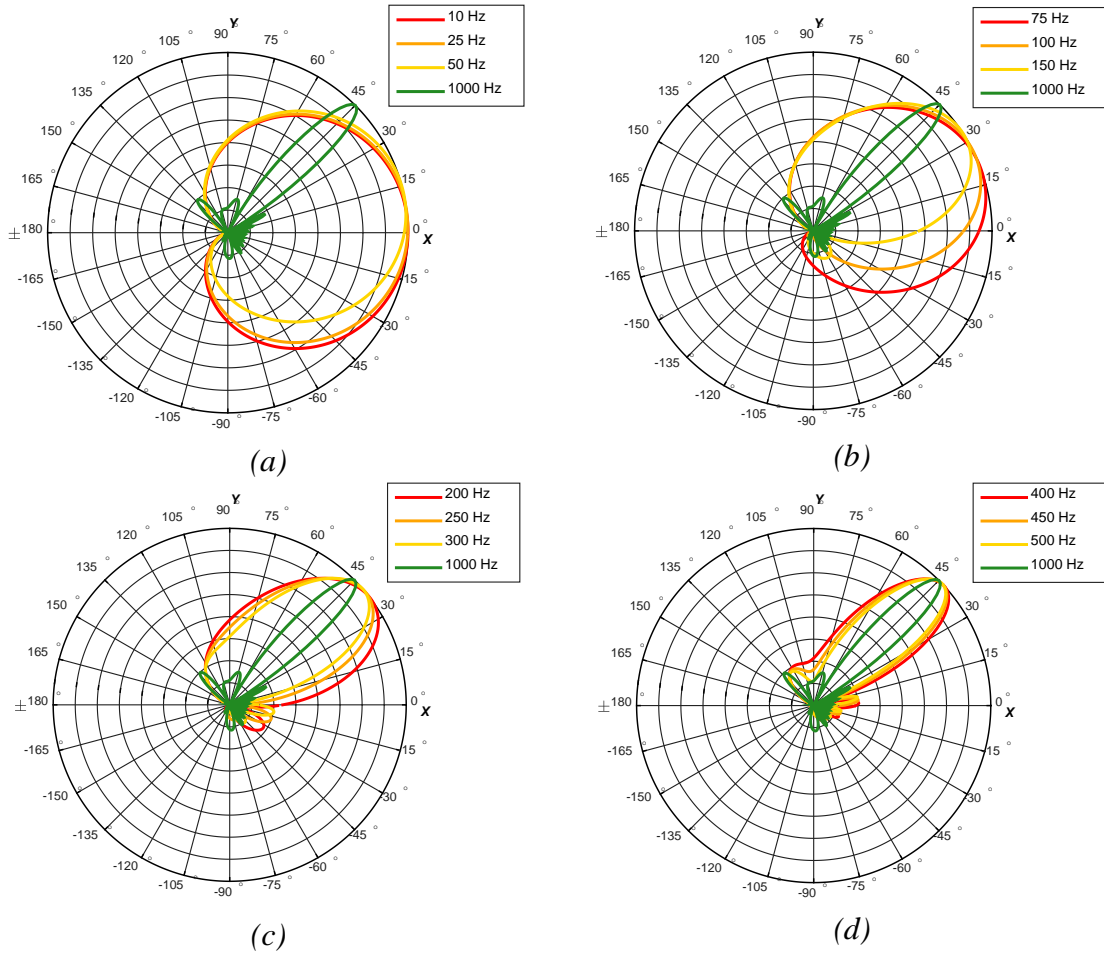
Figure 15   Equalized, horizontal FF beam patterns in the XY plane of a linear array of 11 triplets vs. frequency and bearing angle ψ, steered to 45°.

31

(e)   *(f)*
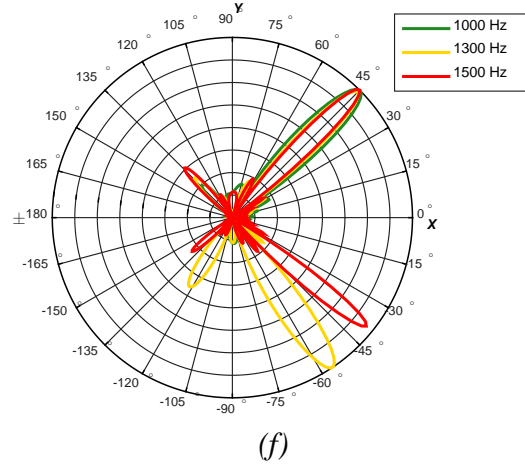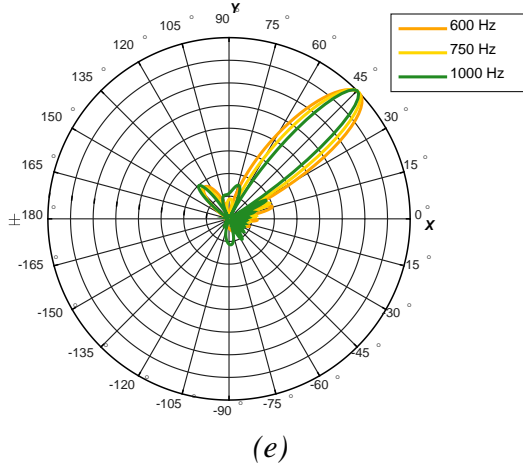
Figure 15. (Continued.)

The last series, shown in Figure 16, with a 60° beam steering, very close to end-fire, indicate that only for f_a the beam pattern matches the steer angle.

(a)   *(b)*
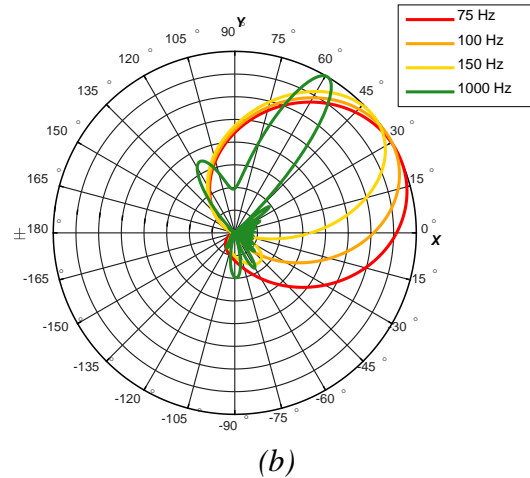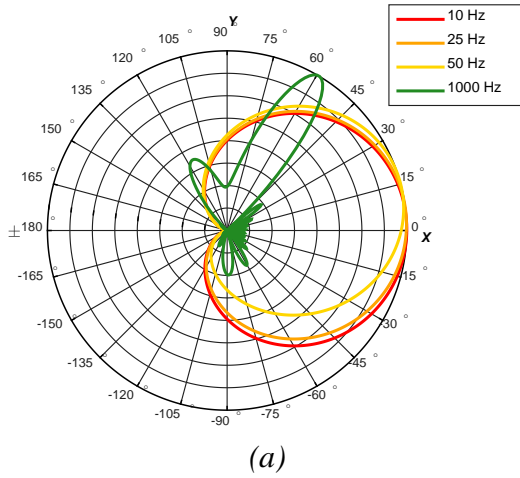
Figure 16   Equalized, horizontal FF beam patterns in the XY plane of a linear array of 11 triplets vs. frequency and bearing angle ψ, steered to 60°.
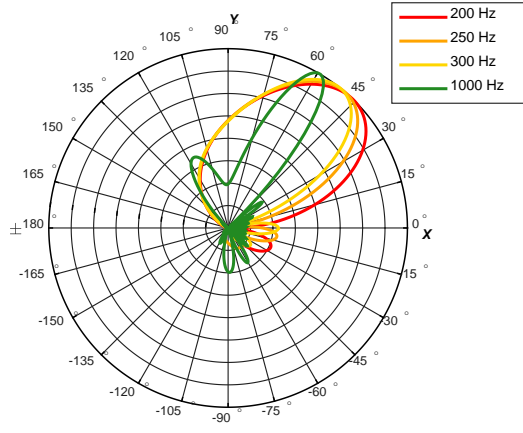
(c)
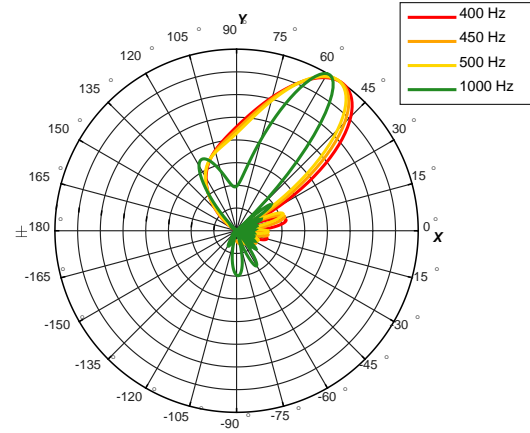
(d)
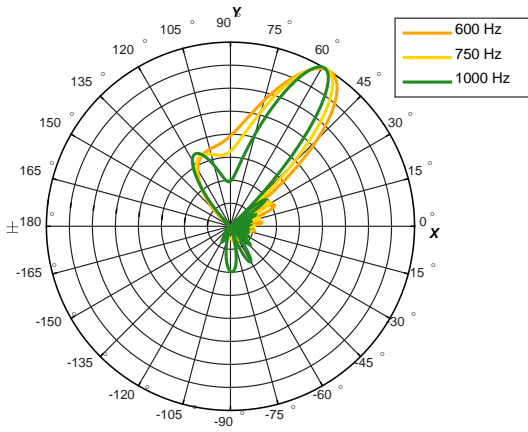
(e)
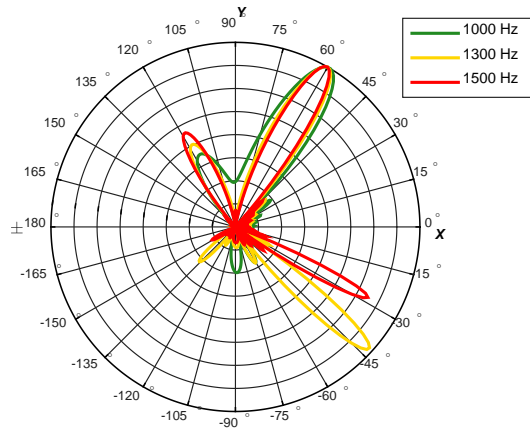
(f)

Figure 16. (Continued.)

The results obtained in this analysis showed that a linear array of eleven single triplets yields a FF beam pattern free of PS ambiguity for the frequency range 10 Hz–1500 Hz [Figure 11(f)], with no beam steering. As the beam pattern is steered towards end-fire, the operational frequency range reduces, pushing the upper limit down to 600 Hz for a beam-steer angle of 45°. For a beam-steer angle of 60°, the beam pattern is distorted for any frequency other than 1000 Hz.

33

THIS PAGE INTENTIONALLY LEFT BLANK

IV.   TWIN-LINE PLANAR ARRAY

This chapter introduces the twin-line planar array, and shows how it solves the PS (port/starboard) ambiguity problem. A study of horizontal FF (far-field) beam patterns as a function of frequency and beam steering demonstrates the operational constraints of a twin-line planar array with fixed spacing between elements. Section C describes how this limitation is usually resolved using sub-arrays.

A.   DEFINITION

The twin-line planar array is composed of two parallel linear arrays with N identical, complex-weighted, omnidirectional point elements per line. Figure 17 shows a twin-line planar array with $N = 6$ lying in the XY plane.

The spacings in the X and Y directions, which equally separate all elements, are denoted by d_X and d_Y, respectively. Following the spatial orientation introduced in Chapter I, the towing direction, starboard side, and port side are indicated by the positive Y axis, positive X axis, and negative X axis, respectively. The element coordinates (x_1, y_n) in the positive X and Y directions, with respect to the origin, are given by [9, Ch. 8, Example 8.2-1]

$$x_1 = 0.5\, d_X \tag{4.1}$$

$$y_n = (n-0.5)\, d_Y , \quad n = 1,\, 2,\, ...,\, N/2 \tag{4.2}$$

and the element coordinates (x_{-1}, y_{-n}) in the negative X and Y directions, with respect to the origin, are given by

$$(x_{-1}, y_{-n}) = (-x_1, -y_n). \tag{4.3}$$
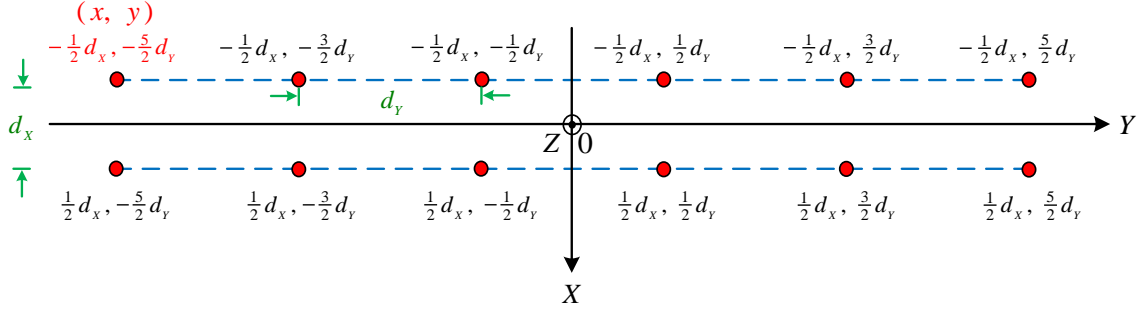
Figure 17   Twin-line planar array lying in the *XY* plane (adapted from [9, Ch. 8, Example 8.2-1], Figure 8.2-2).

Using the Product Theorem, and assuming separable complex weights, the unnormalized, FF beam pattern of the twin-line planar array lying in the *XY* plane is given by [9, Ch. 8, Example 8.2-1]

$$D(f, f_X, f_Y) = \mathbb{S}(f)\, S_X(f, f_X)\, S_Y(f, f_Y) \tag{4.4}$$

where $\mathbb{S}(f)$ is the complex, element sensitivity function, and $S_X(f, f_X)$ and $S_Y(f, f_Y)$ are the array factors in the *X* and *Y* directions, respectively, given by [9, Ch. 8, Example 8.2-1]

$$S_X(f, f_X) = 2\, a_1(f) \cos[\pi(f_X - f_X')d_X] \tag{4.5}$$

$$S_Y(f, f_Y) = 2 \sum_{n=1}^{N/2} b_n(f) \cos[2\pi(f_Y - f_Y')(n - 0.5)d_Y] \tag{4.6}$$

where

$$a_1(f) = a_{-1}(f) \tag{4.7}$$

are the amplitude weights in the positive and negative *X* directions, respectively [9, Ch. 8, Example 8.2-1],

$$b_n(f) = b_{-n}(f), \quad n = 1,\, 2,\, ...,\, N \tag{4.8}$$

are the amplitude weights in the positive and negative *Y* directions, respectively [9, Ch. 8, Example 8.2-1], and f_X and f_Y are the spatial frequencies in the *X* and *Y* directions, respectively, defined by

$$f_X = u / \lambda \qquad (4.9)$$

$$f_Y = v / \lambda \qquad (4.10)$$

and

$$f_X' = u' / \lambda \qquad (4.11)$$

$$f_Y' = v' / \lambda. \qquad (4.12)$$

The beam pattern of the array is steered to $u = u'$ and $v = v'$ in direction-cosine space, where the dimensionless direction cosines with respect to the X direction are given by

$$u = \sin\theta \cos\psi \qquad (4.13)$$

$$u' = \sin\theta' \cos\psi' \qquad (4.14)$$

and the dimensionless direction cosines with respect to the Y direction are given by

$$v = \sin\theta \sin\psi \qquad (4.15)$$

$$v' = \sin\theta' \sin\psi'. \qquad (4.16)$$

Substituting Equations (4.5), (4.6), and (4.9) through (4.12) into Equation (4.4), the unnormalized, FF beam pattern of the twin-line planar array lying in the XY plane becomes [9, Ch. 8, Example 8.2-1]

$$D(f,u,v) = 4\, a_1(f)\, \mathbb{S}(f)\cos\left[\pi(u-u')\frac{d_X}{\lambda}\right] \sum_{n=1}^{N/2} b_n(f)\cos\left[2\pi(v-v')(n-0.5)\frac{d_Y}{\lambda}\right]. \qquad (4.17)$$

B.   HORIZONTAL FF BEAM PATTERNS

The study of the horizontal FF beam patterns in the XY plane employed a twin-line planar array with six elements per line, as shown in Figure 17. The frequency range is the same as that used for the array of triplets—between 10 and 1000 Hz. The array was configured with interelement spacings set to the following values, which yield a beam pattern with no PS ambiguity [9, Ch. 8, Example 8.2-1]

$$d_Y = \lambda_{\min} / 2 \qquad (4.18)$$

$$d_X = \lambda_{\min} / 4 \qquad (4.19)$$

where $\lambda_{\min}$ is the wavelength corresponding to the frequency upper limit $f_{\max} = 1000$ Hz. Since the beam pattern will not be steered to end-fire, the value chosen for d_Y obeys the condition given by Equation (3.1), required to avoid grating lobes. For a horizontal beam pattern in the *XY* plane, both θ and θ' were set to 90° in Equations (4.13) through (4.16).

Figure 18 shows the normalized, horizontal FF beam pattern for the operating frequency set to the optimum value $f_{\max}$, and with no beam steering (ψ' set to zero), which is free of PS ambiguity. Nevertheless, the PS rejection diminishes as the frequency decreases, as observed in Figure 19. For the lowest frequency in this series, 120 Hz (*d*), the array becomes approximately omnidirectional [see Figure 19(d)].
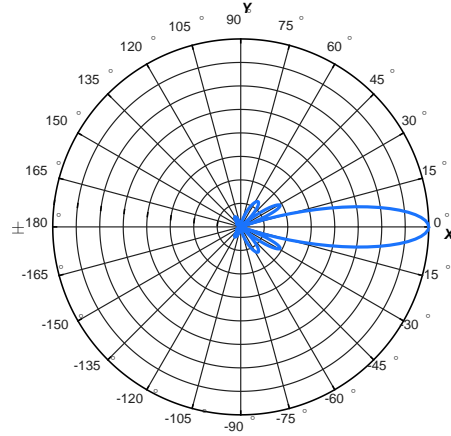
Figure 18   Normalized, horizontal FF beam pattern in the *XY* plane of the twin-line planar array with six elements per line vs. bearing angle ψ, for f = 1000 Hz, with no beam steering.
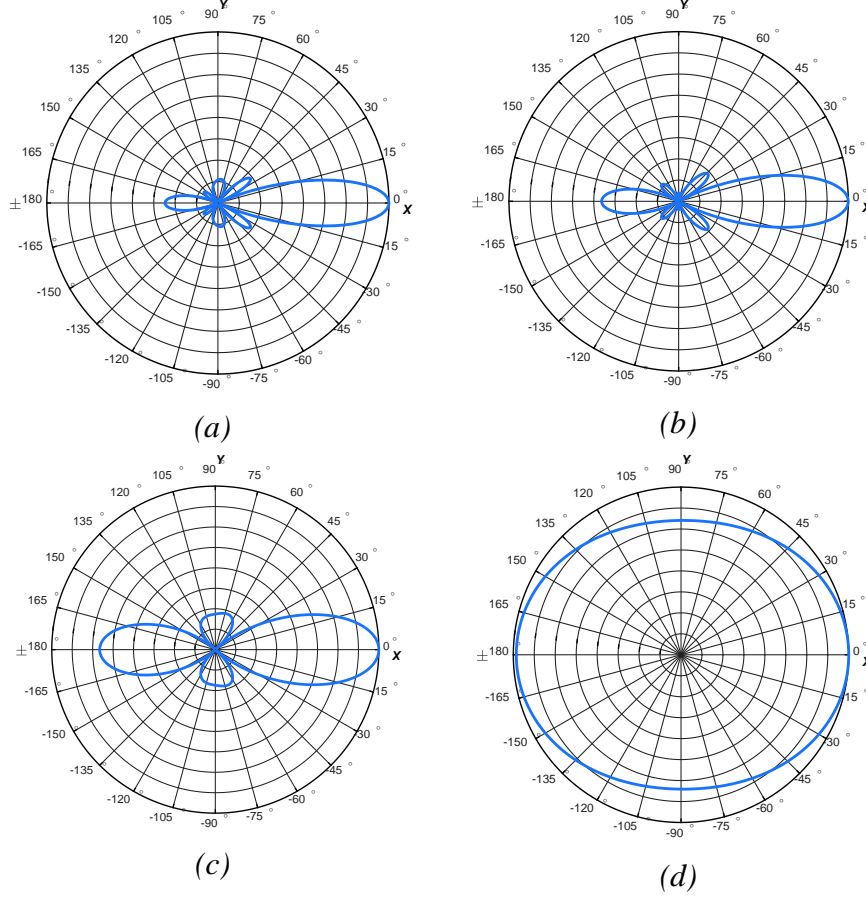
Figure 19   Normalized, horizontal FF beam patterns in the *XY* plane of the twin-
line planar array with six elements per line vs. bearing angle ψ, with no
beam steering, for f equal to (a) 800 Hz, (b) 700 Hz, (c) 500 Hz, and
(d) 120 Hz.

This behavior can be understood by examining the expression for the beam
pattern, when the element spacings defined by Equations (4.18) and (4.19) are substituted
into Equation (4.17), and the angles $\theta = \theta' = 90°$ and $\psi' = 0°$ are substituted into
Equations (4.13) through (4.16), yielding

$$D(f,90°,\psi) = 4\, a_1(f)\,\mathbb{S}(f)\cos[\pi(\cos\psi - 1)\frac{1}{4}\frac{\lambda_{min}}{\lambda}] \sum_{n=1}^{N/2} b_n(f)\cos[\pi(\sin\psi)(n - \frac{1}{2})\frac{\lambda_{min}}{\lambda}].\ (4.20)$$

For small values of the angle ψ, the arguments of the cosine functions in Equation (4.20)
will be close to zero, and the beam pattern will have the highest values. In addition, both
arguments are weighted by the ratio λ_{min}/λ, whose maximum value is 1—corresponding

39

to $f = f_{max}$ and to the narrowest 3-dB beamwidth of the mainlobe—and then decreases as the frequency decreases. Given a range of angles ψ around zero corresponding to the mainlobe at broadside, a decrease in frequency will increase the value $D(f, 90°, \psi)$ computed for each angle ψ in this range, since λ_{min} / λ is decreasing and, hence, increasing the values of both cosine functions. This translates into widening the mainlobe, as observed in Figure 19(c) and (d). Therefore, if one could vary the interelement spacing in the array, such that, for every frequency—or at least for intermediate values within the operational frequency range—the ratio λ_{min} / λ would be equal to 1, then the directivity of the array would be optimized. This concept is the basis of the sub-array technique discussed in the next section.

C.   SUB-ARRAY

A sub-array is a subset of a group of sensors, which constitutes a full twin-line planar array, independent from the remaining sensors. Each sub-array is dimensioned for a given frequency, referred to as the sub-array frequency f_{sa}, and is activated to detect targets with frequency components up to f_{sa}. Figure 20(a) shows an arrangement composed of three sub-arrays [Figure 20(b), (c) and (d)], with 26, 8 and 6 elements per line and interelement spacings in the Y direction d_{Y_1}, d_{Y_2} and d_{Y_3}, respectively, which are related by the integer ratio K_i:

$$K_i = d_{Y_i} / d_{Y_1}, \quad i = 1, 2, 3 \tag{4.21}$$

whose values are $K_1 = 1$, $K_2 = 3$, and $K_3 = 5$. Denoting f_{max} as the frequency corresponding to sub-array 1 and using Equation (4.18), the sub-array frequencies f_{sa_i} are given by

$$K_i = \frac{d_{Y_i}}{d_{Y_1}} = \frac{\lambda_{sa_i} / 2}{\lambda_{sa_1} / 2} = \frac{\lambda_{sa_i}}{\lambda_{min}} = \frac{c / f_{sa_i}}{c / f_{max}} = \frac{f_{max}}{f_{sa_i}} \quad \rightarrow \quad f_{sa_i} = \frac{f_{max}}{K_i}. \tag{4.22}$$

40

Consequently, if sub-array 1 has its spacing d_{Y_1} dimensioned for sub-array frequency f_{sa_1} = 1000 Hz, then sub-arrays 2 and 3 will be suitable for sub-array frequencies f_{sa_2} = 333.3 Hz and f_{sa_3} = 200 Hz, respectively.

In order for the twin-line planar array to locate targets with frequency components up to a given limit F_{MAX}, one should activate the sub-array with f_{sa_i} such that

$$F_{MAX} \leq f_{sa_i} \qquad (4.23)$$

and calculate the beam pattern with frequencies up to F_{MAX} to avoid grating lobes. Therefore, for F_{MAX} equal to 180 Hz, for example, sub-array 3 (f_{sa_3} = 200 Hz) should be activated, and for 900 Hz, sub-array 1 (f_{sa_1} = 1000 Hz) should be activated. Nevertheless, as seen in the previous section, the beam pattern undergoes distortion as the operational frequency gets farther from the frequency used to set the interelement spacing d_{Y_i}. The worst case occurs when F_{MAX} is just above a sub-array frequency. If F_{MAX} is equal to 220 Hz, for example, then the closest sub-array frequency greater than F_{MAX} is f_{sa_2} = 333 Hz (sub-array 2). Thus, the use of this array will yield beam patterns with high sidelobes and low PS rejection within the frequency interval $0 - F_{MAX}$. In this case, a better choice would be to activate sub-array 3, ignoring components above 200 Hz. Additional sub-arrays increase the number of sub-array frequencies, and thus shorten the frequency intervals between them, but represent an increase in the number of elements, raising complexity and costs.

For an inter-element spacing in the Y direction corresponding to f_{max} = 1000 Hz, calculated using Equation (4.18)

$$d_{Y_1} = \lambda_{min} / 2 = c / 2 f_{max} \qquad (4.24)$$

which yields d_{Y_1} = 0.75 m—considering a constant speed of sound equal to 1500 m/sec—this array will have length L_1 given by the following expression:

41
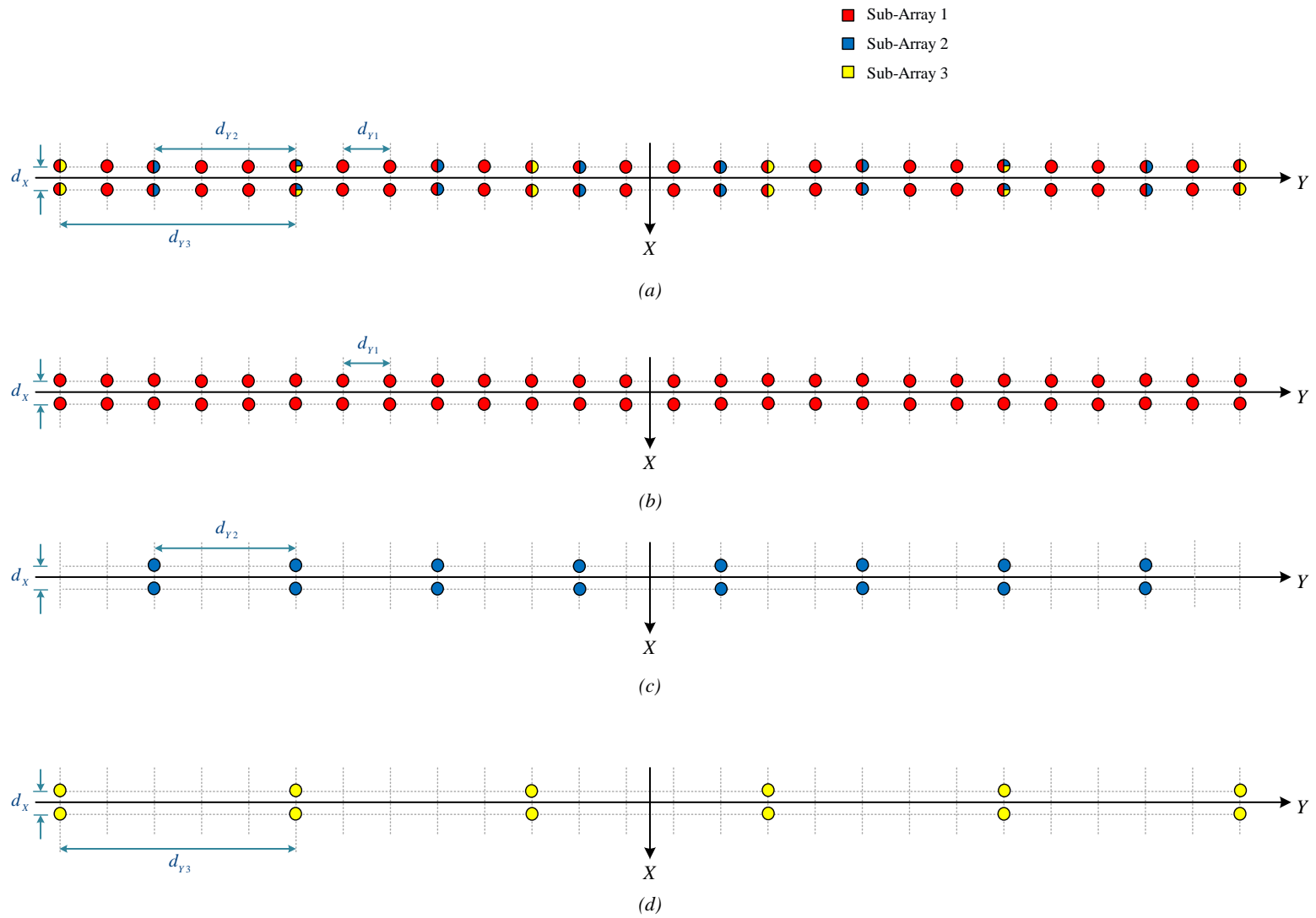
Figure 20   Twin-line planar array using three sub-arrays.

42

$$L_1 = (N_1 - 1)\, d_{Y_1} \tag{4.25}$$

yielding $L_1 = 18.75$ m. Table 2 summarizes the parameters for the three sub-arrays shown in Figure 20. The inter-element spacing d_X in the X direction for the twin-line planar array is equal to 0.375 m, calculated using Equation (4.19).

Table 2   Parameters for the three sub-arrays in Figure 21.

Sub-Array (i)	K_i	d_{Y_i} (m)	d_X (m)	f_{sa_i} (Hz)	N_i
1	1	0.75		1000.0	26
2	3	2.25	0.375	333.3	8
3	5	3.75		200.0	6

Concerning the calculation of the beam pattern, since the interelement spacing d_{Yi} in the Y direction is different by a factor K_i for each sub-array,

$$d_{Y_i} = \lambda_{sa_i} / 2, \quad i = 1, 2, 3 \tag{4.26}$$

but the interelement spacing d_X in the X direction is kept constant, then the condition stated in Equation (4.19) for a beam pattern free of PS ambiguity is violated for the sub-arrays other than the first one, that is:

$$d_{X_i} \neq \lambda_{min} / 4, \quad i = 2, 3 \tag{4.27}$$

where

$$\lambda_{min} = \lambda_{sa_1}. \tag{4.28}$$

This violation can be compensated for by applying, for each sub-array, the corresponding ratio K_i as a weighting factor in the first cosine function of $D(f, u, v)$, given by Equation (4.17), yielding the following expression for the beam pattern $D_i(f, u, v)$ of the ith sub-array:

$$D_i(f,u,v) = 4\,a_1(f)\,\mathbb{S}(f)\cos\left[\pi(u-u')\frac{d_X}{\lambda_{sa_i}}K_i\right]\sum_{n=1}^{N/2}b_n(f)\cos\left[2\pi(v-v')(n-0.5)\frac{d_{Y_i}}{\lambda_{sa_i}}\right].\quad(4.29)$$

Since K_i is equal to $\lambda_{sa_i}/\lambda_{sa_1}$ [see Equation (4.22)], one can notice that, even using the same interelement spacing d_X in all sub-arrays, the expression for $D_i(f,u,v)$ is equivalent to

$$D_i(f,u,v) = 4\,a_1(f)\,\mathbb{S}(f)\cos\left[\pi(u-u')\frac{d_X}{\lambda_{sa_1}}\right]\sum_{n=1}^{N/2}b_n(f)\cos\left[2\pi(v-v')(n-0.5)\frac{d_{Y_i}}{\lambda_{sa_1}}\right]\quad(4.30)$$

which matches both conditions stated in Equations (4.18) and (4.19) for PS ambiguity rejection:

$$d_{Y_i} = \lambda_{sa_i}/2 \tag{4.31}$$

$$d_X = \lambda_{sa_1}/4. \tag{4.32}$$

D.   HORIZONTAL FF BEAM PATTERNS USING SUB-ARRAYS

The following series of horizontal FF beam patterns, calculated using Equation (4.29), illustrates the application of the twin-line planar array with three sub-arrays dimensioned in the last section at frequencies f_{sa_i} equal to 1000, 333.3 and 200 Hz (see Table 2). The first series was calculated with no beam steering. Afterwards, a specific sub-array is used, in order to investigate the effect of steering.

1.   No Beam Steering

The series of beam patterns shown in Figure 21 confirms the effectiveness of the sub-array technique, evaluated at operational frequencies 140 Hz (a), 180 Hz (b), 220 Hz (c), and 900 Hz (d). The first two frequencies are processed by sub-array 3 (f_{sa_3} = 200 Hz), the third one by sub-array 2 (f_{sa_2} = 333.3 Hz), and the last one by sub-array 1 (f_{sa_1} = 1000 Hz). For operational frequencies close to and less than a sub-array frequency—for example, 180 Hz $\leq$ f_{sa_3} = 200 Hz and 900 Hz $\leq$ f_{sa_1} = 1000 Hz—the beam patterns show

very small sidelobes, while at intermediate frequencies far from and less than sub-array frequencies—for example, 140 Hz $\le f_{sa_3} = 200$ Hz and 220 Hz $\le f_{sa_2} = 333.3$ Hz—very pronounced sidelobes were observed, as expected.
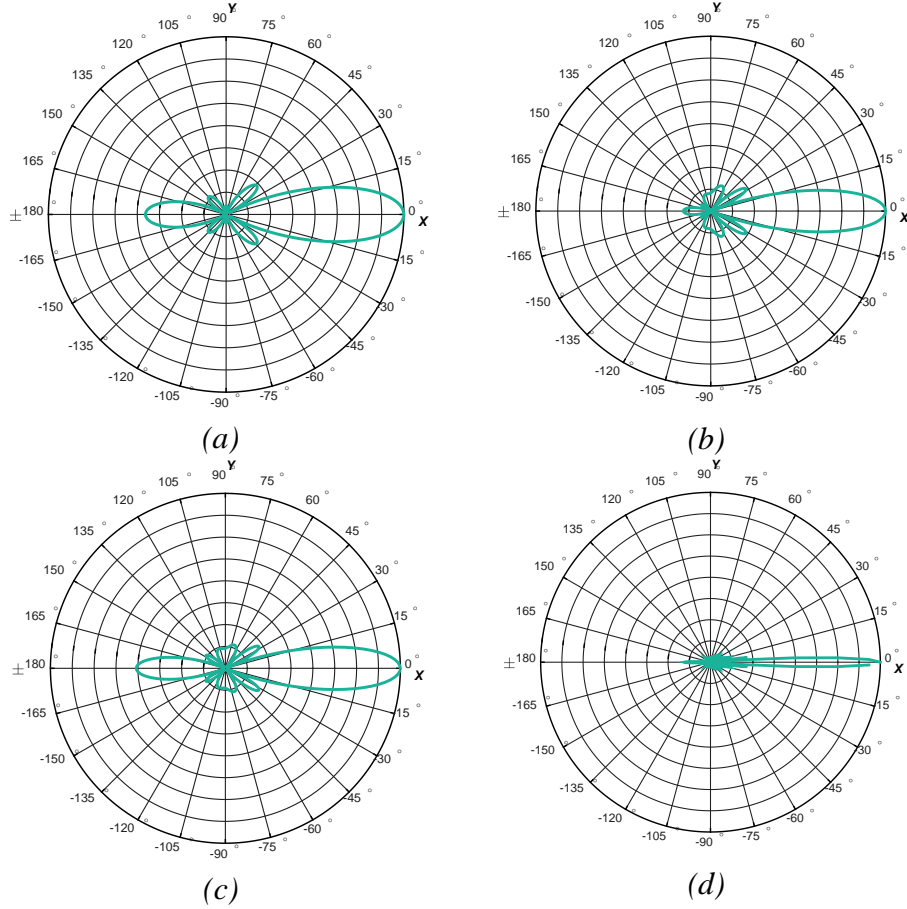
Figure 21   Normalized, horizontal FF beam patterns in the *XY* plane of the twin-line planar array vs. bearing angle ψ, using sub-arrays, with no beam steering, for operational frequencies (a) 140 Hz, (b) 180 Hz, (c) 220 Hz, and (d) 900 Hz.

2.   With Beam Steering

The beam pattern becomes distorted when steered towards end-fire, as shown for the sub-array frequency of 200 Hz in Figure 22. Up to a beam-steer angle of 30° [Figure 22(c)] the beam pattern is virtually free of significant sidelobes. By further steering to 50° [Figure 22(e)], the increase in the 3-dB beamwidth of the mainlobe is noticeable and the

beam pattern is badly distorted. The steering limit determined above is lowered when the twin-line planar array operates at non-sub-array frequencies, since their beam patterns with no steering already have noticeable sidelobes [see Figure 21(a) and (c)].

The combined effects of non-sub-array frequencies and steering is shown in Figure 23 for the worst case considered previously—the operational frequency set to 220 Hz. Above a beam-steer angle of 15°, as illustrated in Figure 23(c) and (d), the sidelobe approaches the mainlobe in magnitude, such that the array loses its PS rejection ability for that frequency. Therefore, additional sub-arrays are needed to allow for a greater beam-steer angle while preserving PS rejection.

(a)   *(b)*

(c)   *(d)*
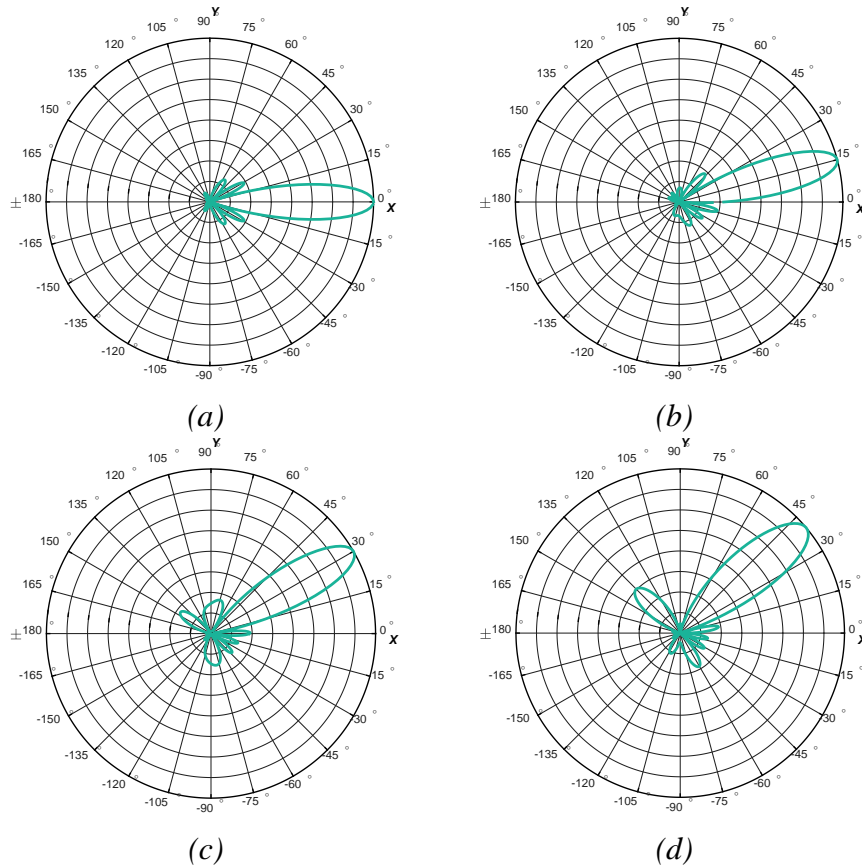
Figure 22   Normalized, horizontal FF beam patterns in the *XY* plane of the twin-line planar array vs. bearing angle ψ , using a sub-array frequency of 200 Hz, and beam steered to (a) 0°, (b) 15°, (c) 30°, (d) 40° and (e) 50°.

46
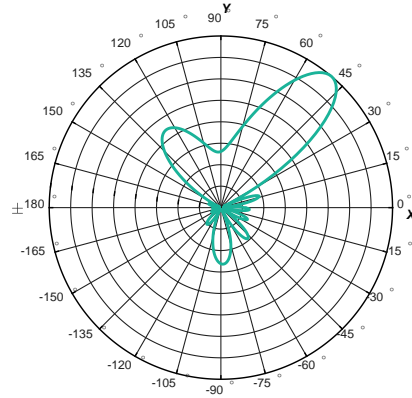
(e)

Figure 22. (Continued.)
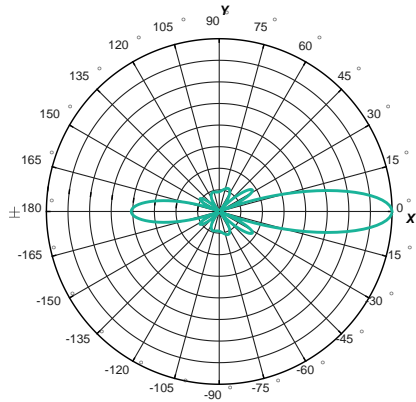
(a)
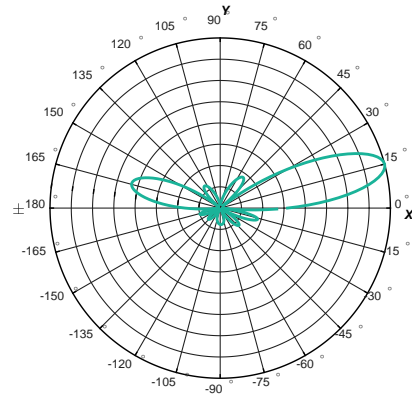
(b)
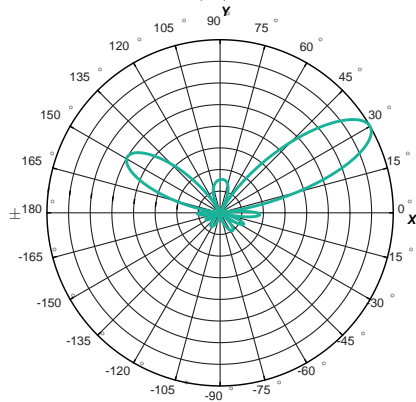
(c)
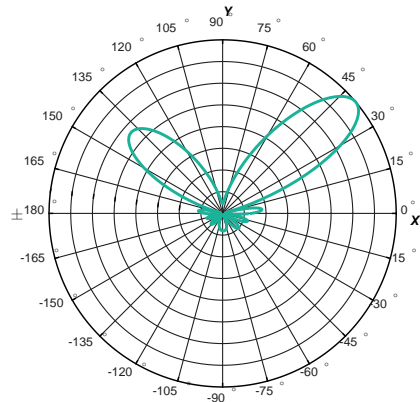
(d)

Figure 23   Normalized, horizontal FF beam patterns in the *XY* plane of the twin-line planar array vs. bearing angle ψ, using a sub-array frequency of 220 Hz, and beam steered to (a) 0°, (b) 15°, (c) 30°, and (d) 40°.

47

This section concludes the modeling and testing of the twin-line planar array except for the transduction and the beamforming, which require an input acoustical signal, and thus will be presented in the Chapter V along with the sound-source simulation. The twin-line planar array segmentation into sub-arrays, discussed in this Chapter, will not be utilized in Chapter VI. The original twin-line planar array with N equal to six elements per line studied in Section A will be used instead, and the focus will be on signal processing.

V. SIGNAL GENERATOR AND FFT BEAMFORMING

This chapter describes the signal generator, which is a simulation of a sound-source and the transmission medium, used to evaluate the performance of the twin-line planar array. The generator depends upon the properties of the medium being simulated, and the physical arrangement of elements along the array. Therefore, this generator is specific to a twin-line planar array, and both of them create an interdependent system. Nevertheless, the methodology is generic and can be applied as well for the array of triplets or other types of sonar arrays, by simply changing the code associated with the sonar array.

The system composed by the signal generator and the twin-line planar array has three modules, as shown in Figure 24: the sound-source, the medium and the array, which are discussed in Sections A through C, respectively. They are bound by a common parameter, the range between each array element and the sound-source. The two main system outputs are the beamformed signal—generated using the FFT beamforming method (presented in Section D)—and the beam pattern, calculated using a two-dimensional spatial DFT (described in Section E).

A. SOUND-SOURCE

The basic purpose of the signal generator is to verify if the twin-line beamformer under development and testing is working properly, that is, if it estimates the correct bearing angle of a target whose coordinates are known.

Therefore, for testing purposes, an omnidirectional point-source with adjustable spherical coordinates and radiating an acoustic signal consisting of a deterministic, noise-free, single frequency, CW (continuous wave) pulse was used to model the target. Once the beamformer is validated, one might extend the generator to multiple sources located at different coordinates, and using deterministic or random, CW or modulated signals, such as LFM (linear frequency-modulated) or HFM (hyperbolic frequency-modulated) signals.
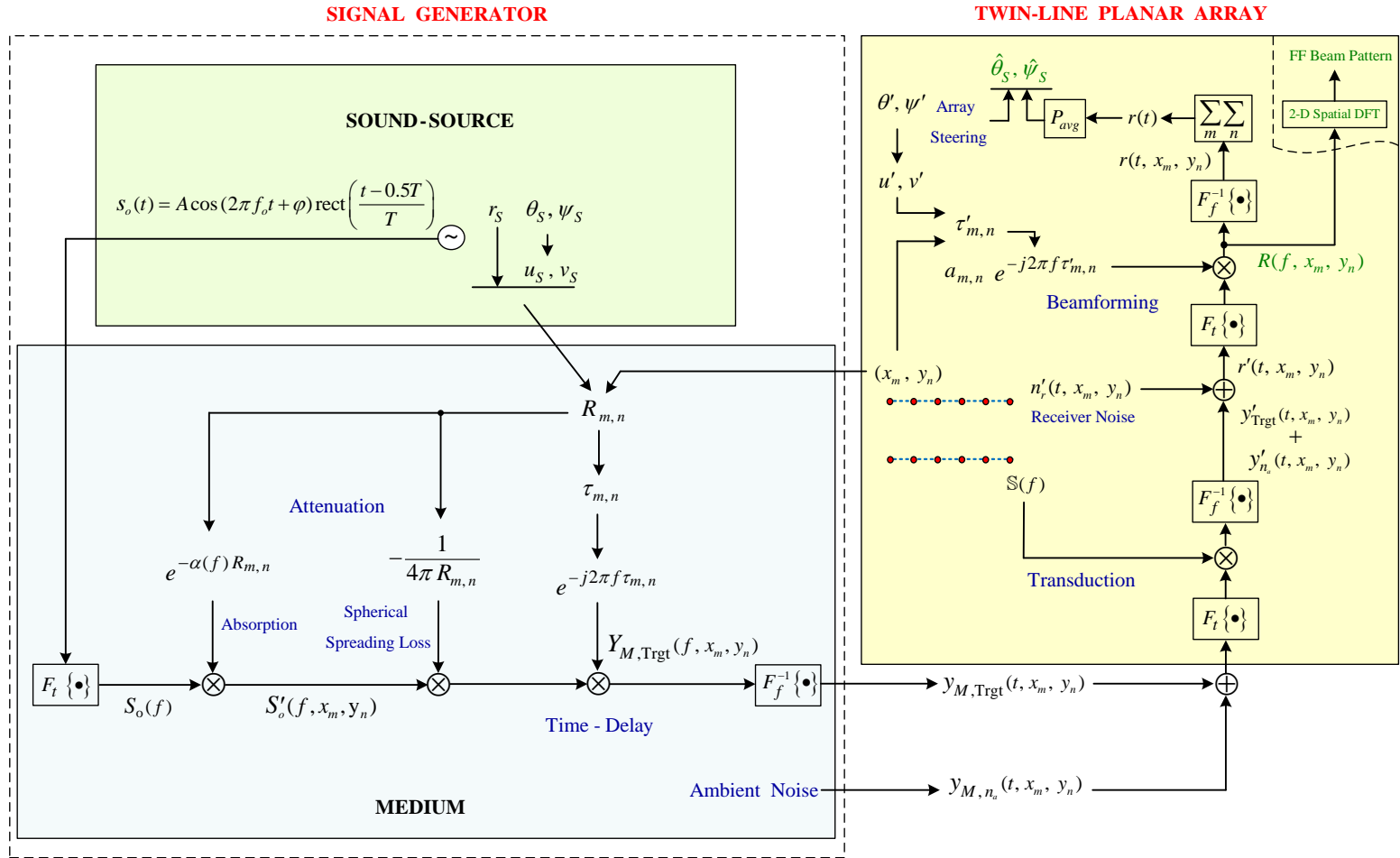
Figure 24   System composed of the signal generator and the twin-line planar array (based on [9, Sec. 7.2–7.4 and Sec. 8.5]).

The target's source strength $s_o(t)$ (volume flow rate, in m^3/sec) is given by a rectangular-envelope, CW with pulse length T (sec), amplitude A (in m^3/sec), carrier frequency f_o (in Hz), and phase φ (in rad):

$$s_o(t) = A\cos(2\pi f_o t + \varphi)\,\text{rect}\left(\frac{t - 0.5T}{T}\right) \tag{5.1}$$

where

$$\text{rect}\left(\frac{t - 0.5T}{T}\right) = \begin{cases} 1, & 0 \le t \le T \\ 0, & \text{otherwise}. \end{cases} \tag{5.2}$$

The amplitude A can be calculated from the pressure amplitude P (in Pa) at a distance r from the center of the source and as a function of frequency f (in Hz) using the following expression [10]

$$A = 2\frac{\lambda r}{\rho_o c} P \quad \rightarrow \quad A = \frac{2r}{f\,\rho_o} P \tag{5.3}$$

where ρ_o is the constant ambient density of the fluid in kg/m^3, and c is the speed of sound in the fluid in m/sec. The sound pressure level SPL in dB relative to the reference pressure amplitude P_{ref}, that is, SPL re P_{ref}, is given by [10, p. 130]

$$SPL = 20\log(P / P_{ref}), \tag{5.4}$$

where P_{ref} is equal to 1μPa.

Therefore, a given range of radiated noise level (RNL) in dB re 1μPa as a function of frequency f, taken from a target's acoustical signature, can be used to calculate the amplitude source strength at $r = 1$ m generated by a sound-source simulating that target. Solving Equation (5.4) for pressure P, replacing SPL with RNL, and substituting P in Equation (5.3) yields

$$A\big|_{r=1m} = \frac{2}{f\,\rho_o} P_{ref} \text{ x } 10^{RNL(f)/20}. \tag{5.5}$$

51

The complex frequency spectrum of the target's source strength $S_o(f)$ (in (m³/sec)/Hz) is given by

$$S_o(f) = F_t\{s_o(t)\}. \tag{5.6}$$

The omnidirectional, point target, located at spherical coordinates (r_S, θ_S, ψ_S), is shown in Figure 25 along with the twin-line planar array lying in the XY plane. The range $R_{m,n}$ in meters between the target and the center of the array element with rectangular coordinates (x_m, y_n) is given by [9, Sec. 8.5]

$$R_{m,n} = \sqrt{r_S^2 - 2r_S(u_S x_m + v_S y_n) + x_m^2 + y_n^2} \tag{5.7}$$

where

$$r_S = \sqrt{x_S^2 + y_S^2 + z_S^2} \tag{5.8}$$

$$u_S = \sin\theta_S \cos\psi_S \tag{5.9}$$

$$v_S = \sin\theta_S \sin\psi_S. \tag{5.10}$$
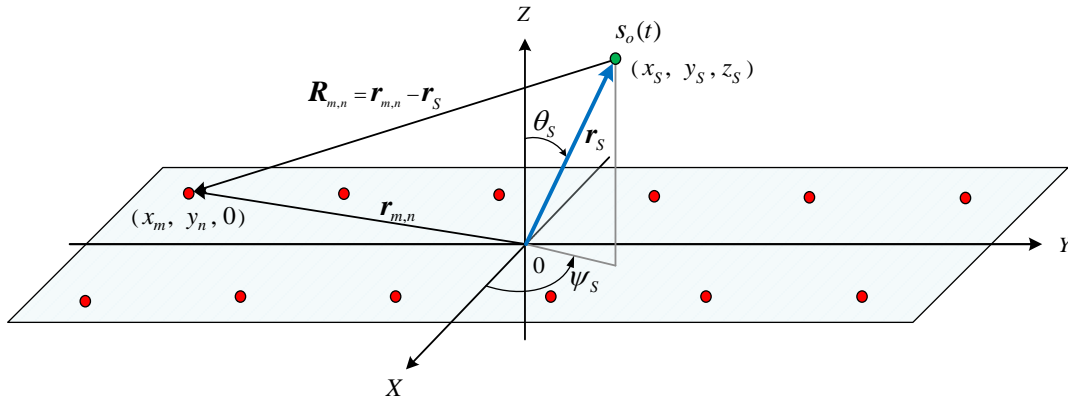
Figure 25   Sound-source and the twin-line planar array lying in the XY plane.

The signal generator assumes the coordinates of both the twin-line planar array and target to be constant, that is, there is no motion, and hence, no Doppler shift (frequency shift due to relative motion).

B.   MEDIUM

For the purpose of testing, a simple model was used for the fluid medium (seawater) with the following characteristics:

- Unbounded: the acoustic field radiated by the target has no interaction with the ocean surface or bottom.

- Viscous: the sound waves are subject to fluid resistance, which causes absorption of sound energy, subsequently dissipated as heat. This absorption is frequency-dependent and is quantified by the attenuation coefficient $\alpha'(f)$, which varies also with temperature and salinity, but can be approximated by [11]

$$\alpha'(f) = \left(\frac{0.08}{0.9 + F^2} + \frac{30}{3000 + F^2} + 4 \times 10^{-4} \right) F^2 \qquad (5.11)$$

where F is the frequency in kHz, and $\alpha'(f)$ is in dB/km.

The attenuation coefficient $\alpha'(f)$ in dB/km can be converted to Np/m by using the following expression [9, Sec. 7.2], which is plotted for the frequency interval 0 to $f_s / 2$ in Figure 26

$$\alpha(f) = \frac{\alpha'(f)}{8.686 \times 10^3}. \qquad (5.12)$$
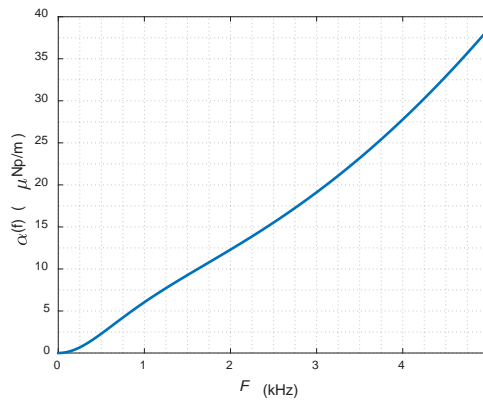
Figure 26   Attenuation coefficient $\alpha(f)$ in Np/m vs. frequency in kHz.

53

- Homogeneous: there is no sound speed variation with depth, density and temperature, which would cause the sound waves to refract along their trajectory towards the twin-line planar array. The sound waves propagate spherically through the medium at a constant speed c (in m/sec).

Following the sequence of operations performed by the medium as shown in Figure 24, the first step is absorption. Since the absorption coefficient $\alpha(f)$ is frequency-dependent, this operation must be carried out in the frequency-domain, i.e., the coefficient must be applied to the complex frequency spectrum of the target's source strength $S_o(f)$. The total absorption is the product of $\alpha(f)$, in Np/m, and the range $R_{m,n}$, such that [9, Sec. 7.2–7.4 and Sec. 8.5]

$$S_o'(f, x_m, y_n) = S_o(f) e^{-\alpha(f)R_{m,n}}. \tag{5.13}$$

The next two steps, attenuation by spherical spreading loss, and the time delay experienced by the signal, are combined in the following expression for the complex frequency spectrum, in $(m^2/sec)/Hz$, of $y_{M,Tgrt}(t, x_m, y_n)$—the velocity potential of the spherical wave propagating in the medium [9, Sec. 7.2–7.4 and Sec. 8.5]

$$Y_{M,Trgt}(f, x_m, y_n) = -\frac{1}{4\pi R_{m,n}} S_o'(f, x_m, y_n) \, e^{-j2\pi f \tau_{m,n}} \tag{5.14}$$

where $\tau_{m,n}$ (in sec) is the one-way time delay perceived by the array element separated by the distance $R_{m,n}$ from the sound source and is given by

$$\tau_{m,n} = R_{m,n} / c. \tag{5.15}$$

The velocity potential, $y_{M,Trgt}(t, x_m, y_n)$, in m^2/sec, can be written as follows, and constitutes the first output of the signal generator shown in Figure 24 [9, Sec. 7.2–7.4 and Sec. 8.5]

$$y_{M,Trgt}(t, x_m, y_n) = -\frac{1}{4\pi R_{m,n}} s_o'(t - \tau_{m,n}). \tag{5.16}$$

These three steps are independent, and thus do not need to follow the sequence presented above. In the actual implementation, the target's source strength $s_o(t)$ was generated using a time-shifted version of Equation (5.1) to include the time-delay of each array element, yielding $s_o(t - \tau_{m,n})$. To this signal, absorption and spherical spreading loss were applied.

The second output of the medium module is the velocity potential of the acoustic signal due to ambient noise $y_{M,n_a}(t, x_m, y_n)$, in m²/sec. In deep water, the ambient noise consists predominantly of sound produced by distant ship traffic and distant storms, both in the frequency range 50–500 Hz [1, p. 207].

This model, used along with the single sound-source, provides a simple and controllable test set for the twin-line planar array, such that most of the variables during the development are related to the array.

C.   TWIN-LINE PLANAR ARRAY

The twin-line planar array module performs basically two functions: transduction and beamforming/beam steering, as shown in Figure 24. First, the two signals coming from the medium, $y_{M,Trgt}(t, x_m, y_n)$ and $y_{M,n_a}(t, x_m, y_n)$, are converted to the frequency-domain $\left(F_t\{\bullet\}\right)$, and then multiplied by the complex receiver sensitivity function $\mathbb{S}(f)$, in V/(m²/sec), which quantifies the conversion of acoustical energy into electrical energy by the transducer element. The function $\mathbb{S}(f)$ is determined from the open circuit receiving response of the transducer, which is a curve of the receiver sensitivity level, $RSL(f)$ in dB re RS_{ref}, vs. frequency (in Hz), where the reference receiver sensitivity RS_{ref} is usually equal to 1V/µPa for underwater transducers. The magnitude of $\mathbb{S}(f)$ is given by [9, Appendix 6B]

$$\left|\mathbb{S}(f)\right| = 2\pi f \rho_o RS(f) \tag{5.17}$$

where $RS(f)$ is the receiver sensitivity, given by [9, Appendix 6B]

$$RS(f) = RS_{ref} 10^{RSL(f)/20} \tag{5.18}$$

and ρ_o is the constant ambient density of the fluid, in kg/m^3.

The complex frequency spectrum of the output electrical signal from the element (m, n) in the array due to the target before complex weighting, in V/Hz, is given by [9, Sec. 7.2–7.4 and Sec. 8.5]

$$Y'_{Trgt}(f, x_m, y_n) = Y_{M,Trgt}(f, x_m, y_n) \, \mathbb{S}(f), \tag{5.19}$$

and the complex frequency spectrum due to ambient noise, in V/Hz, is given by [9, Sec. 7.2–7.4 and Sec. 8.5]

$$Y'_{n_a}(f, x_m, y_n) = Y_{M,n_a}(f, x_m, y_n) \, \mathbb{S}(f). \tag{5.20}$$

Both spectra are converted to the time-domain, in order to introduce the receiver additive noise $n'_r(t, x_m, y_n)$. This self-noise consists basically of thermal white noise (AWGN) originated in the receiver's electronic devices, and transduced turbulent pressures (flow noise), created in the turbulent layer around the hydrophones, which introduces a fluctuating noise voltage [1, p. 360].

The resultant noise $z(t, x_m, y_n)$ at each array element is given by the sum of the ambient noise and the receiver noise, given in V by

$$z(t, x_m, y_n) = F_f^{-1}\{Y'_{n_a}(f, x_m, y_n)\} + n'_r(t, x_m, y_n) \tag{5.21}$$

$$z(t, x_m, y_n) = y'_{n_a}(t, x_m, y_n) + n'_r(t, x_m, y_n). \tag{5.22}$$

In the simulator, $z(t, x_m, y_n)$ is created by a Gaussian random number generator, assuming that $y'_{n_a}(t, x_m, y_n)$ and $n'_r(t, x_m, y_n)$ are statistically independent, zero-mean random processes, and is given by

$$z(t, x_m, y_n) = \sigma_z \, z_o(t, m, n) \tag{5.23}$$

where $z_o(t, m, n)$ is the zero-mean, variance one, normal-distributed random sequence generated for element (m, n), and σ_z is the standard deviation of $z(t, x_m, y_n)$ required to

yield a given SNR (in dB) relative to $y'_{Trgt}(t,\, x_m,\, y_n)$. The standard deviation σ_z is given by (see Appendix)

$$\sigma_z = \sqrt{P_{avg,\, y'_{Trgt}}} \, \text{x} \, 10^{-SNR/20} \tag{5.24}$$

where the time-average power $P_{avg,\, y'_{Trgt}}$ of $y'_{Trgt}(t,\, x_m,\, y_n)$, in W-$\Omega$, is given by

$$P_{avg,\, y'_{Trgt}} = \frac{1}{T} \int_0^T \left| y'_{Trgt}(t,\, x_m,\, y_n) \right|^2 dt. \tag{5.25}$$

A different seed is used to generate a random sequence $z_o(t, m, n)$ for each array element, to ensure that the output noise at each element is uncorrelated.

The received electrical signal (in V) at the output of element $(m,\, n)$ in the array before complex weighting, $r'(t,\, x_m,\, y_n)$, is then given by

$$r'(t,\, x_m,\, y_n) = y'_{Trgt}(t,\, x_m,\, y_n) + z(t,\, x_m,\, y_n). \tag{5.26}$$

The next step is the beamforming, or phase alignment of the signals coming from all elements to form a single beam. This process uses as inputs the steer angles $(\theta',\, \psi')$, and the element coordinates $(x_m,\, y_n)$ to calculate the time-delay $\tau'_{m,\, n}$, which, in turn, holds the following relationship with the phase weight $\theta_{m,\, n}$ [9, Sec. 8.2]

$$\tau'_{m,\, n} = - \frac{\theta_{m,\, n}(f)}{2\pi f}. \tag{5.27}$$

Ideally, for the purpose of exactly compensating for the time-delay imposed on the signal during its trajectory towards different elements in the array, one should apply a time delay $\tau'_{m,\, n}$ equal to $\tau_{m,\, n}$ in order to cophase all the signals. In practice, however, the range $R_{m.n}$ is unknown at reception, and $\tau'_{m,\, n}$ cannot be calculated using Equation (5.15).

If the range to the target r_S satisfies the Fraunhofer (far-field) range criterion [9, Sec. 3.1 and 3.2]

$$r_S > \frac{\pi}{\lambda} R_A^2 > 2.414 R_A \qquad (5.28)$$

where the maximum radial extent of the aperture R_A (the twin-line planar array) is given by

$$R_A = \sqrt{\left(\frac{L_X}{2}\right)^2 + \left(\frac{L_Y}{2}\right)^2} \qquad (5.29)$$

where

$$L_X = d_X \qquad (5.30)$$

is the length of the array in the X direction and

$$L_Y = (N-1) d_Y \qquad (5.31)$$

is the length of the array in the Y direction, then [9, Sec. 8.2]

$$\tau'_{m,n} = \frac{u'}{c} x_m + \frac{v'}{c} y_n \qquad (5.32)$$

where

$$u' = \sin(\theta')\cos(\psi') \qquad (5.33)$$

$$v' = \sin(\theta')\sin(\psi'). \qquad (5.34)$$

The complex weights required to cophase the output electrical signals from of all array elements are given by [9, Sec. 8.2]

$$c_{m,n}(f) = a_{m,n} e^{-j2\pi f \tau'_{m,n}} \qquad (5.35)$$

where $a_{m,n}$ are the amplitude weights.

The complex frequency spectrum (in V/Hz) of the received electrical signal at the output of element (m, n) in the array after complex weighting is calculated by converting $r'(t, x_m, y_n)$ in (5.26) to the frequency domain and multiplying by the complex weights [9] yielding

$$R(f, x_m, y_n) = [\, Y'_{Trgt}(f, x_m, y_n) \,+\, Z(f, x_m, y_n) \,]\; c_{m,n}(f). \tag{5.36}$$

This resulting spectrum $R(f, x_m, y_n)$ is used to calculate the FF beam pattern of the array, as will be seen in Section E. The corresponding received electrical signal (in V), is obtained by computing the inverse Fourier transform of $R(f, x_m, y_n)$ as:

$$r(t, x_m, y_n) = F_f^{-1}\{R(f, x_m, y_n)\}. \tag{5.37}$$

Once cophased, the outputs can be summed up with (ideally) no destructive interference, yielding the resultant received electrical signal at the output of the twin-line planar array, $r(t)$ —the beamformed signal.

In order to search for targets, the array's FF beam pattern can be steered by varying the steering angles θ' and ψ', while the signal $r(t)$ is monitored. The coordinates (θ', ψ') at which the time-average power P_{avg} of $r(t)$, in W-Ω, given by

$$P_{avg,\, r} = \frac{1}{T}\int_0^T |r(t)|^2 \, dt, \tag{5.38}$$

reaches its maximum value corresponds to the estimates $(\hat{\theta}_S, \hat{\psi}_S)$ of the target's location.

For the purpose of testing, the target was positioned in the *XY* plane ($\theta_S = 90°$), and the steering was executed only in the *XY* plane ($\theta = 90°$ and $\theta' = 90°$), while ψ' was varied from 0° to 359°, in steps of one degree. Alternatively, instead of evaluating the average power sequentially, for every angle ψ', this operation can be carried out simultaneously for all angles ψ' at once, using parallel signal processing.

D.   FFT BEAMFORMING

Throughout the description of the signal generator, multiple conversions from time to frequency-domain, and vice-versa, using forward $\left(F_t\{\bullet\}\right)$ and inverse $\left(F_f^{-1}\{\bullet\}\right)$ Fourier transforms, are performed. Since all signals $x(t)$ being processed are sampled, both conversions use forward and inverse discrete Fourier transforms (DFT and IDFT, respectively).

Given a continuous-time signal $x(t)$ with frequency spectrum $X(f)$, and its discrete-time version $x(l)$ obtained using a sampling frequency f_s, an estimate $\hat{X}(q)$ of $X(f)$ is given by [9, Sec. 8.5]

$$\hat{X}(q) = T_s \, DFT\{x(l)\} = T_s \sum_{l=0}^{L-1} x(l) W_{L+Z}^{-ql}, \qquad q = -L'', \dots, 0, \dots, L'' \qquad (5.39)$$

$$T_s = 1/f_s \qquad (5.40)$$

$$f = q f_o \qquad (5.41)$$

$$Z = \frac{1}{f_o T_s} - L \qquad (5.42)$$

$$L'' = \begin{cases} (L+Z)/2, & L+Z \ \text{even} \\ (L+Z-1)/2, & L+Z \ \text{odd} \end{cases} \qquad (5.43)$$

$$W_{L+Z} = e^{j\frac{2\pi}{L+Z}} \qquad (5.44)$$

where T_s is the sampling period in sec, L is the number of samples of $x(l)$, q is the DFT bin number, f_o is the desired DFT bin spacing, and Z is the integer number of zeros required for f_o. The inverse Fourier transform of $\hat{X}(q)$ is given by [9, Sec. 8.5]

$$x(l) = \frac{1}{T_s} IDFT\left\{\hat{X}(q)\right\} = \frac{1}{T_s}\frac{1}{L+Z} \sum_{q=-L''}^{L''} \hat{X}(q) W_{L+Z}^{+ql}, \qquad l = 0, 1, \dots, L+Z-1. \quad (5.45)$$

In the actual implementation, both forward and inverse discrete Fourier transforms are evaluated using forward and inverse fast Fourier transform algorithms (FFT and IFFT).

The beamforming step of the signal processing algorithm discussed in Section C starts with the received electrical signal $r'(t, x_m, y_n)$ given by Equation (5.26) and rewritten below sampled at the rate of f_s Hz:

$$r'(t_l, x_m, y_n) = y'_{Trgt}(t_l, x_m, y_n) + z'(t_l, x_m, y_n) \qquad (5.46)$$

$$t_l = lT_s = 1/f_s, \qquad l = 0, 1, \ldots, L-1 \tag{5.47}$$

where t_l is the sampling time instant (in sec). The estimate of the complex frequency spectrum of $r'(t_l, x_m, y_n)$ at discrete frequencies $f = qf_o$ is calculated from Equation (5.39) yielding

$$\hat{R}'(q, x_m, y_n) \equiv \hat{R}'(q f_o, x_m, y_n) = \hat{R}'(f, x_m, y_n)\big|_{f=qf_o}. \tag{5.48}$$

The discrete version of the complex weights required to cophase the output electrical signals can be obtained from Equation (5.35) as follows:

$$c_{m,n}(q f_o) = a_{m,n} e^{-j2\pi q f_o \tau'_{m,n}}. \tag{5.49}$$

Next, the beamforming process is accomplished by multiplying $\hat{R}'(q, x_m, y_n)$ by the complex weights given by Equation (5.49), yielding

$$\hat{R}(q, x_m, y_n) = \hat{R}'(q, x_m, y_n) c_{m,n}(q f_o) \tag{5.50}$$

$$\hat{Z}(q, x_m, y_n) = \hat{Z}'(q, x_m, y_n) c_{m,n}(q f_o). \tag{5.51}$$

Using Equations (5.36), (5.19), (5.14) and (5.13), $\hat{R}(q, x_m, y_n)$ can be rewritten as [9, Sec. 8.5]

$$\hat{R}(q, x_m, y_n) = \hat{S}(q, x_m, y_n)\, a_{m,n}\, e^{-j2\pi q f_o(\tau_{m,n} + \tau'_{m,n})} + \hat{Z}(q, x_m, y_n) \tag{5.52}$$

where $\hat{S}(q, x_m, y_n)$ is an estimate of the theoretical frequency spectrum

$$S(f, x_m, y_n) = -\frac{1}{4\pi R_{m,n}} S_o(f) \mathbb{S}(f)\, e^{-\alpha(f) R_{m,n}} \tag{5.53}$$

and $\hat{Z}(q, x_m, y_n)$ is the estimate of the frequency spectrum of noise after beamforming. In addition, for a target located in the FF region of the twin-line planar array, the sum $\tau_{m,n} + \tau'_{m,n}$ in Equation (5.52) can be approximated by [9, Sec. 8.5]

$$\tau_{m,n} + \tau'_{m,n} \approx \tau_S + \frac{1}{c}(u' - u_S)m\,d_X + \frac{1}{c}(v' - v_S)m\,d_Y \tag{5.54}$$

61

where τ_S is the one-way time-delay between the target and the center of the array in sec, and u_S and v_S are the target's direction cosines.

Both $\hat{R}(q, x_m, y_n)$ and its inverse DFT, the received electrical signal $r(l, x_m, y_n)$, can be used to estimate the position of a target, as the beam pattern of the array is steered. As discussed in Section C, the cophased signals $r(l, x_m, y_n)$ can be summed, yielding the resultant output electrical signal $r(l)$, whose time-average power is calculated by

$$P_{avg,r} = \frac{1}{L}\sum_{l=0}^{L-1}|r(l)|^2 . \tag{5.55}$$

The steer angles (θ', ψ') corresponding to the output electrical signal $r(l)$ with maximum time-average power will be the estimates $(\hat{\theta}_S, \hat{\psi}_S)$ of the target's location.

The frequency spectrum $\hat{R}(q, x_m, y_n)$ can be used to calculate the FF beam pattern of the twin-line planar array, which can also indicate the location of the target, by monitoring its maximum magnitude as the beam pattern is steered, as will be explained in Section E.

E.   BEAM PATTERNS USING TWO-DIMENSIONAL SPATIAL FFT

In Chapter IV, where the behavior of the FF beam pattern of the twin-line planar array was studied in terms of frequency and steer angle, $D(f,\theta,\psi)$ was calculated in a specific plane—the XY plane, in which the twin-line planar array lies—by setting θ and θ' equal to 90° and varying ψ. For a given frequency f, $|D(f, 90°, \psi)|$ was plotted vs. angle ψ.

In this Chapter the beam patterns are plotted as a function of both direction cosines u and v, which, as will be shown, allows determining the target's location from the beam patterns as they are being steered. The two-dimensional spatial DFT computes the beam pattern as a function of both direction cosines, and is calculated by computing the spatial DFT of $\hat{R}(q, x_m, y_n)$ in the X direction, referred to as DFT_m, and then uses

this result to compute the spatial DFT in the *Y* direction, referred to as DFT_n—though the order of computations can be reversed [9, Sec. 8.5].

The spatial DFT_m of $\hat{R}(q,\, x_m,\, y_n)$ in the *X* direction yields the frequency-and-angular spectrum estimate $\hat{\mathcal{R}}(q,\, r,\, n)$ given by the following expression, used for linear arrays with an even number of elements [9, Appendix 6E]

$$\hat{\mathcal{R}}(q,\, r,\, n) = W_{M'+Z_X}^{r/2} \sum_{m=1}^{M'} \hat{R}(q,\, x_m,\, y_n) W_{M'+Z_X}^{-rm} \;+\; W_{M'+Z_X}^{-r/2} \sum_{m=1}^{M'} \hat{R}(q,\, x_m,\, y_n) W_{M'+Z_X}^{rm}, \qquad (5.56)$$

where

$$W_{M'+Z_X} = e^{+j\frac{2\pi}{M'+Z_X}} \qquad (5.57)$$

$$r = -M'',\, \ldots,\, 0,\, \ldots,\, M'' \qquad (5.58)$$

is the DFT bin number corresponding to discrete spatial frequency $f_X = r\,\Delta f_X$,

$$M'' = \begin{cases} (M' + Z_X)/2, & M' + Z_X \text{ even} \\ (M' + Z_X - 1)/2, & M' + Z_X \text{ odd} \end{cases} \qquad (5.59)$$

$$M' = M\,/\,2 \qquad (5.60)$$

$$\Delta f_X = \frac{1}{(M' + Z_X)d_X} \qquad (5.61)$$

is the spatial-frequency spacing in the *X* direction (in cycles/m),

$$Z_X = \frac{1}{\delta u}\frac{\lambda}{d_X} - M' \qquad (5.62)$$

where δu is a desired direction cosine u bin spacing, and Z_X is the integer number of zeros required to obtain δu.

The next step consists of using $\hat{\mathcal{R}}(q,\, r,\, n)$ as input to calculate the spatial DFT_n in the *Y* direction, yielding the frequency-and-angular spectrum estimate $\hat{R}(q,\, r,\, s)$. The calculation makes use of the same expressions given by Equations (5.56) through (5.62),

63

with $\hat{R}(q, x_m, y_n)$ replaced with $\hat{\mathcal{R}}(q, r, n)$, M with N, M' with N', M'' with N'', r with s, Δf_X with Δf_Y, Z_X with Z_Y, d_X with d_Y, and δu with δv.

The magnitude of the function $\hat{R}(q, r, s)$ is proportional to the far-field beam pattern of the twin-line planar array [9, Sec. 8.5]. The DFT bin numbers r and s are related to direction cosines u_r and v_s as follows [9, Sec. 8.3]:

$$u_r = \frac{r}{M + Z_X} \frac{\lambda}{d_X} \tag{5.63}$$

$$v_s = \frac{s}{N + Z_Y} \frac{\lambda}{d_Y}. \tag{5.64}$$

Recalling that the input for the two-dimensional spatial DFT, $\hat{R}(q, x_m, y_n)$, depends on the sum $\tau_{m,n} + \tau'_{m,n}$ given by Equation (5.54), $\hat{R}(q, r, s)$ is steered in the direction [9, Sec. 8.5]

$$u = u_{r'} = u' - u_S \tag{5.65}$$

and

$$v = v_{s'} = v' - v_S \tag{5.66}$$

in direction-cosine space, where r' and s' are the DFT bin numbers corresponding to the location of the maximum value of $\left|\hat{R}(q, r, s)\right|$. The normalized magnitude of $\hat{R}(q, r, s)$ is plotted as a function of direction cosines u and v, as illustrated by the density plots in Figure 27. With no beam steering, that is, $u' = 0$ and $v' = 0$, the maximum magnitude of $\hat{R}(q, r, s)$ is located at $(-u_S, -v_S)$, as shown in Figure 27(a). Using correct beam steering, that is, $u' = u_S$ and $v' = v_S$, the maximum magnitude of $\hat{R}(q, r, s)$ is located at $(0,0)$, as shown in Figure 27(b).
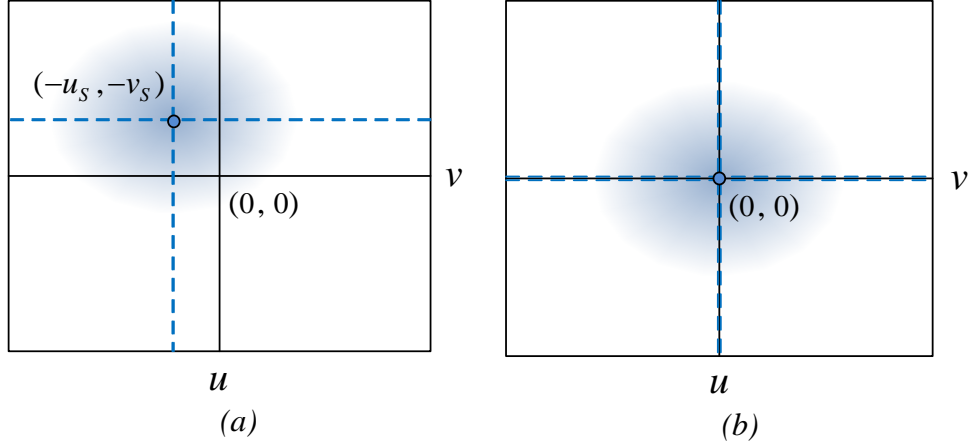
Figure 27   Normalized magnitude of $\hat{R}(q,\, r,\, s)$ as a function of direction cosines u and v, (a) with no beam steering) and (b) using correct beam steering.

The estimates $(\hat{\theta}_S, \hat{\psi}_S)$ can be calculated from the direction cosines $(u_{r'}, v_{s'})$ corresponding to the peak of the density plot with no beam steering in Figure 27(a), using the following expressions [9, Sec. 8.5]

$$\hat{\theta}_S = \frac{180°}{\pi} \sin^{-1}\left(\sqrt{(u_{r'})^2 + (v_{s'})^2}\right), \qquad \sqrt{(u_{r'})^2 + (v_{s'})^2} \leq 1 \qquad (5.67)$$

$$\hat{\psi}_S = \frac{180°}{\pi} \tan^{-1}\left(v_{s'} / u_{r'}\right). \qquad (5.68)$$

This chapter concludes the theoretical description of the twin-line planar array, and its association with an acoustic signal coming from a simulated target and propagated through a simple model for the medium. The deployment of this system will be discussed in Chapter VI.

65

THIS PAGE INTENTIONALLY LEFT BLANK

VI.   SIGNAL GENERATOR SIMULATIONS

This chapter demonstrates the use of the system composed of the signal generator and the twin-line planar array to estimate the position of a target. The results will be presented as two-dimensional beam patterns.

A.   SIGNAL GENERATOR SETTINGS

The following parameters and assumptions for medium, twin-line planar array and target were adopted.

1.   Medium

The sound speed c is set to 1500 m/s, and the density ρ_o of seawater is approximated to 1000 kg/m^3.

2.   Twin-Line Planar Array

The model of the twin-line planar array with $N = 6$ elements per line lying in the *XY* plane sketched in Figure 17 is employed here. The array is dimensioned for a maximum operational frequency $f_{max} = 1000$ Hz, which has been considered throughout this text. Using Equations (4.18) and (4.19), the interelement spacings d_X and d_Y are equal to 0.375 m and 0.750 m, respectively, and the maximum radial extent of the aperture R_A is equal to 1.884 m, calculated from Equation (5.29).

The elements of the modeled twin-line planar array are assumed to have a RSL approximately constant in the frequency range of operation, which is set to 10–1000 Hz. For wideband-receiver transducers, the typical range for a RSL is between -220 dB and -190 dB re 1V/μPa [12]. Considering the operational frequency range and the model's assumption for the array sensors to be omnidirectional point elements, a reasonable reference of RSL to be used in the simulation can be taken from the Cetacean Research™'s C55 hydrophone datasheet [13]. This transducer is omnidirectional below 10 kHz [13] and has a RSL approximately constant in the range 20–1000 Hz, as shown in Figure 28. Based on this receiving response, a constant RSL equal to -167 dB re 1V/μPa

is adopted. Using Equation (5.18), this value corresponds to a RS equal to $10^{-8.35}$ V/µPa, and the magnitude of the receiver sensitivity function $\mathbb{S}(f)$ defined in Equation (5.17) reduces to

$$\left|\mathbb{S}(f)\right| = 2 \times 10^{-5.35}\,\pi f. \tag{6.1}$$
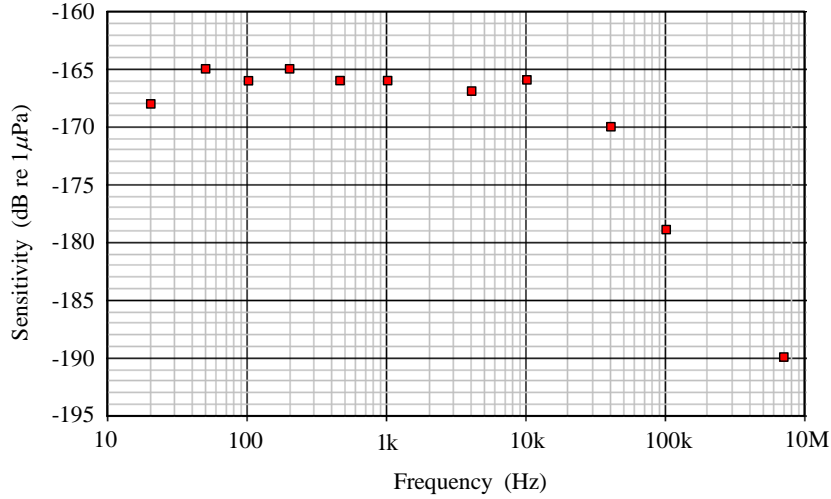
Figure 28   Receiving response of the Cetacean Research™'s C55 hydrophone
(adapted from [13]).

3.   Sound-Source

The function generator simulating the acoustical signal radiated by the target produces a rectangular-envelope CW pulse, given by Equation (5.1), 500 msec in length, A m^3/sec in amplitude, sampled at f_s = 10 kHz, with carrier frequency f_o adjustable within the frequency range 10–1000 Hz, and with null phase φ. Therefore, the target's source strength defined by Equation (5.1) and expressed in m^3/sec becomes,

$$s_o(t) = A\cos\left(2\pi 1000t\right)\mathrm{rect}\left(\frac{t - 0.5T}{T}\right). \tag{6.2}$$

The order of magnitude of the noise level radiated by a modern diesel submarine at low speed (4 knots) at 1 kHz and 1 m is 120 dB re 1µPa [12, p. 115]. Therefore, using Equation (5.5), the corresponding source strength's amplitude A is given by

68

$$A = \frac{2}{10^3 \text{x} 10^3} 1\text{x} 10^{-6} \text{x} \, 10^{120/20} \quad \rightarrow \quad A = 2\text{x} 10^{-6} \, \text{m}^3/\text{sec}. \tag{6.3}$$

The target is an omnidirectional, point source, as discussed in the theoretical model, and the range to the target r_S is set to 500 m. Substituting r_S and the lower limit of operational wavelength, $\lambda_{\min} = 1.5$ m, into the expression for the Fraunhofer (FF) range criterion, Equation (5.28), results in

$$r_S \; (500\,\text{m}) > \frac{\pi}{\lambda} R_A^2 \; (7.44\,\text{m}) > \; 2.414\,R_A \; (4.55\,\text{m}), \tag{6.4}$$

ensuring that the sound-source is in the FF region of the twin-line planar array, and thus validating the value chosen for r_S. The target is positioned in the *XY* plane ($\theta_S = 90°$), and the beam steering will be executed only in the *XY* plane ($\theta = 90°$ and $\theta' = 90°$), while ψ' will be varied from $0°$ to $359°$.

B. SIMULATIONS

Using the parameter values set above for the signal generator and the twin-line planar array, simulations were performed for the carrier frequency $f_o = 1000$ Hz and two scenarios: no noise and signal plus noise. Two opposite cases were considered initially for the target's bearing angle ψ_S: closer to broadside ($\psi_S = 15°$), which corresponds to a very directive beam pattern, and closer to end-fire ($\psi_S = 55°$), with a prominent sidelobe at $125°$, as shown in Figure 29(a) and (b), respectively.

(a)   *(b)*
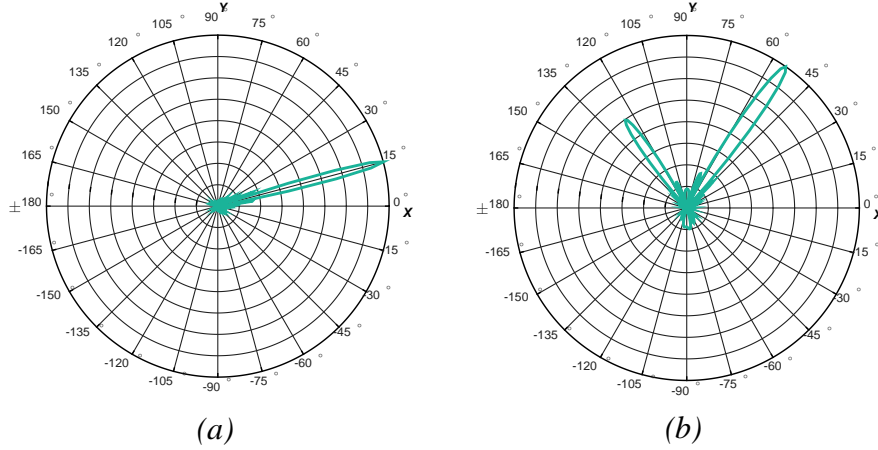
Figure 29   Normalized, horizontal FF beam patterns in the *XY* plane of the twin-
line planar array vs. bearing angle ψ, for the carrier frequency 1000 Hz,
and beam steered to (a) 15° and (b) 55°.

1.   Target's Bearing Angle Estimation based on Time-Average Power

a.   Target at $\psi_S = 15°$

The sequence of plots of the time-average power of the received electrical signal
$r(t)$ shown in Figure 30 were obtained by steering the beam pattern of the array from ψ'
= 0° to 359°, in steps of 0.1°. The plots correspond to $r(t)$ free of noise [Figure 30(a)],
and corrupted by noise with SNR equal to +3 dB [Figure 30(b)], 0 dB [Figure 30(c)] and
–3 dB [Figure 30(d)] respectively. The very low level of time-average power of these
signals (on the order of 10^{-18}) is due to the fact that a pre-amplifier block for the received
signal was not modeled.

Figure 30   Time-average power (in W-Ω) of $r(t)$ vs. bearing angle ψ' for the
target located at $\psi_S = 15°$, with (a) no noise, (b) SNR = +3 dB, (c) SNR
= 0 dB and (d) SNR = –3 dB.

For the SNR = 0 dB and +3 dB cases considered, the time-average power peaks
exactly at $\psi' = 15°$. In the worst scenario (SNR = –3 dB)—illustrated in Figure 31 with a
plot of $y'_{Trgt}(t,1,2)$ and its noise-corrupted version, $r'(t,1,2)$, for array element (1,2)—the
time-average power peak is at $\psi' = 14.9°$. This good performance lies in the fact that
when the beamformed signals $r(t, x_m, y_n)$ are summed to yield $r(t)$, the weak, cophased
signals due to the target contained in $r(t, x_m, y_n)$ add constructively to create a strong
signal, while the zero-mean noise signal's contributions average out approximately to

71

zero. Additionally, the remaining noise is eliminated during the calculation of the time-average power of $r(t)$.
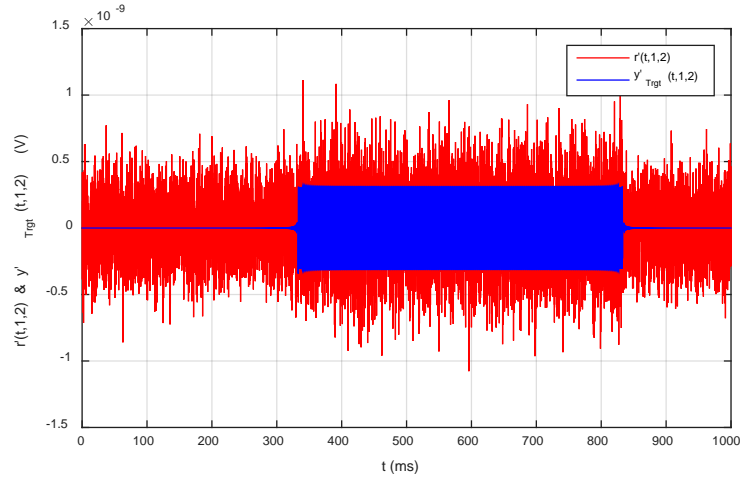
Figure 31   Received electrical signal from element (1, 2) before complex weighting [$r'(t,1,2)$ in red], in V, and output electrical signal from element (1, 2) due to the target only before complex weighting [$y'_{Trgt}(t,1,2)$ in blue], in V, versus time t , in msec.

b.   Target at $\psi_S = 55^\bullet$

With the target's bearing angle ψ_S set to 55°, a similar behavior relative to SNR was observed, as illustrated in the plots of the time-average power of $r(t)$ vs. bearing angle ψ' in Figure 32. Contrasting the case of $\psi_S = 15°$, there are two outstanding side peaks, located at 119.4° and 273° in the plot with no additive noise [Figure 32(a)]. The first side peak was expected, since the beam pattern steered to 55° shows a sidelobe at 125° [see Figure 29(b)].

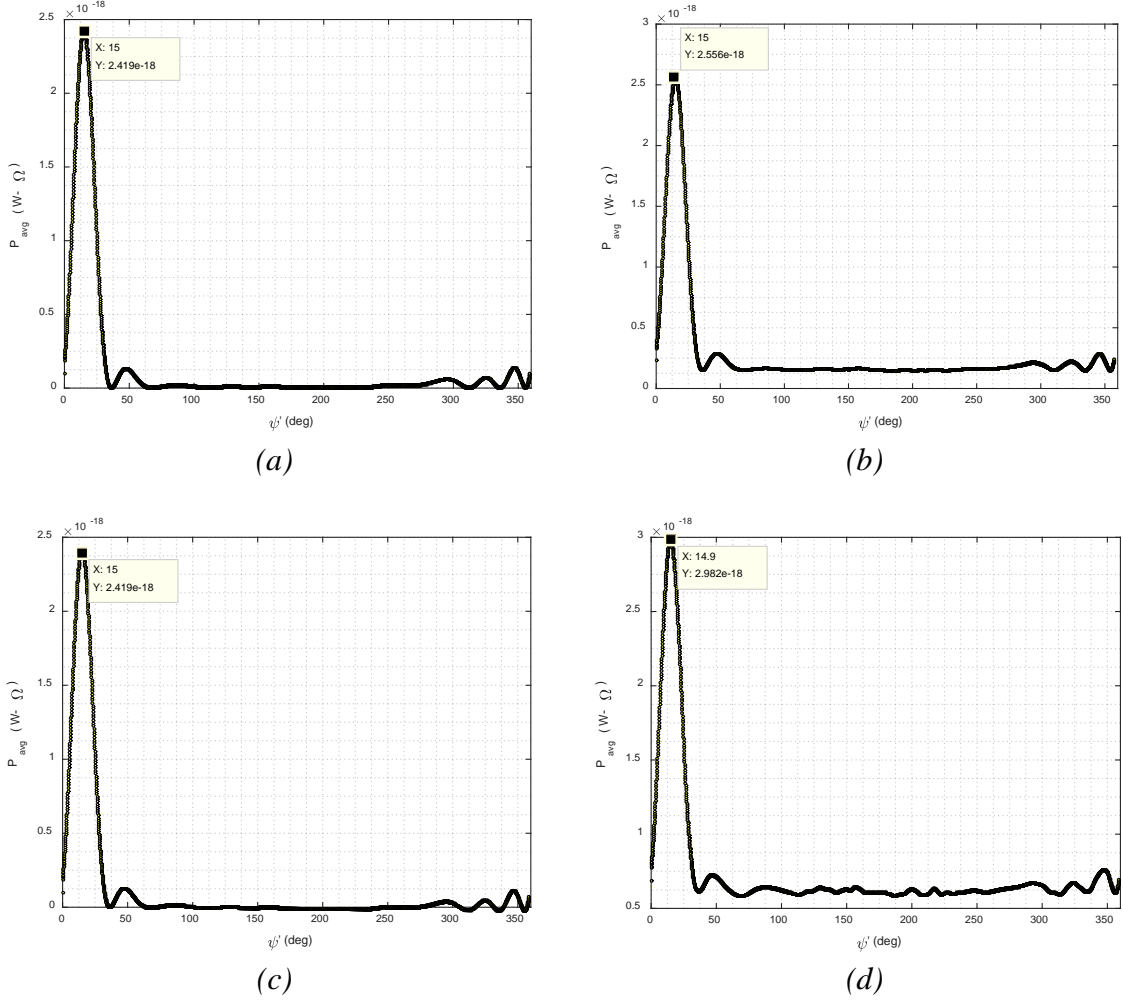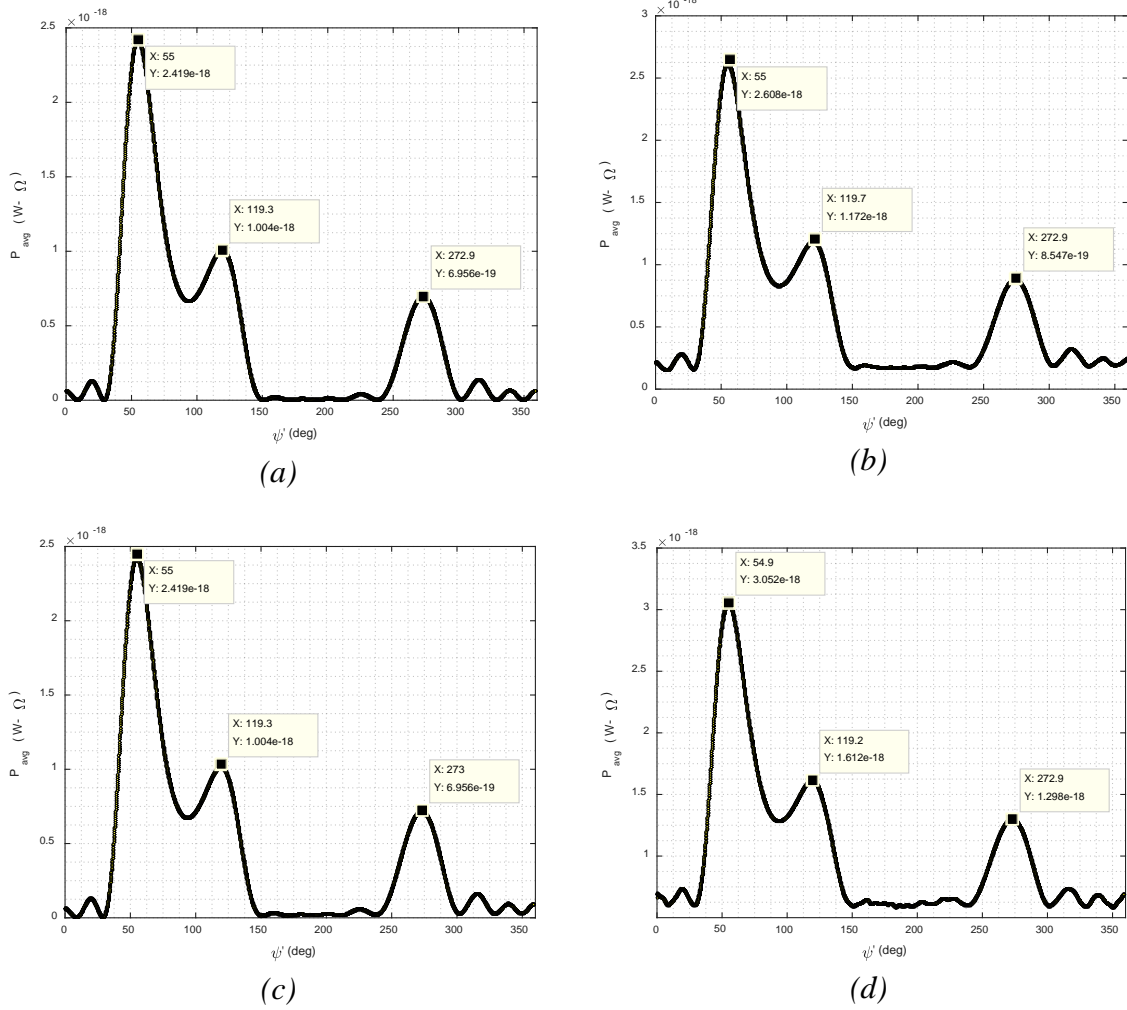Figure 32   Time-average power (in W-Ω) of $r(t)$ vs. bearing angle ψ' for the target located at $\psi_S = 55°$, with (a) no noise, (b) SNR = +3 dB, (c) SNR = 0 dB and (d) SNR = −3 dB.

Since the side peaks are far lower in magnitude than the main peak located at $\psi' = 55°$, the maximum time-average power criterion for the estimation of ψ_S still holds at $\psi_S = 55°$ with a reasonable margin. These results also indicate that the initially adopted steer limit of 55° could be potentially extended farther towards end-fire. Therefore, two additional simulations were performed for the target at $\psi_S = 65°$ and 75° (but only for the limiting cases—no noise and SNR = −3 dB), with the results plotted in Figure 33 and Figure 34, respectively, to test this hypothesis.
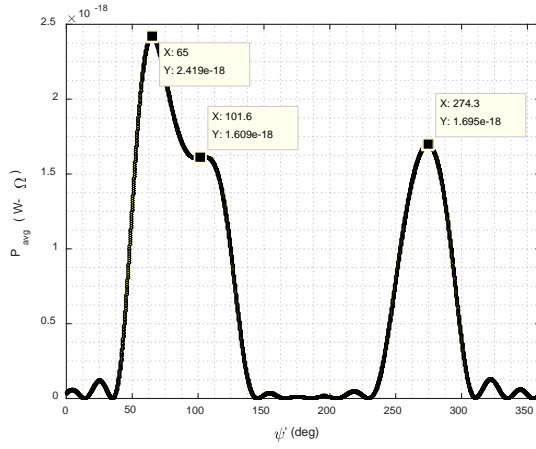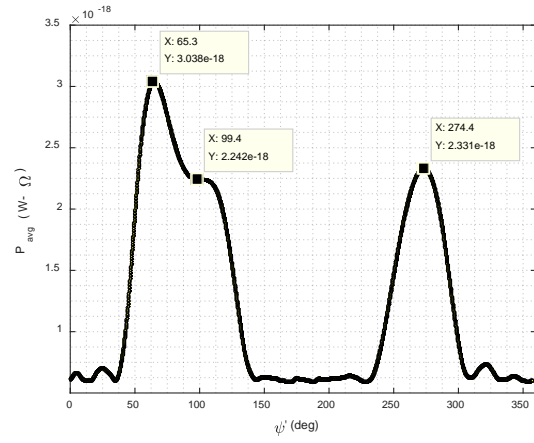
(a)   *(b)*

Figure 33   Time-average power (in W-Ω) of $r(t)$ vs. bearing angle ψ' for the target located at $\psi_S = 65°$, with (a) no noise and (b) SNR = –3 dB.
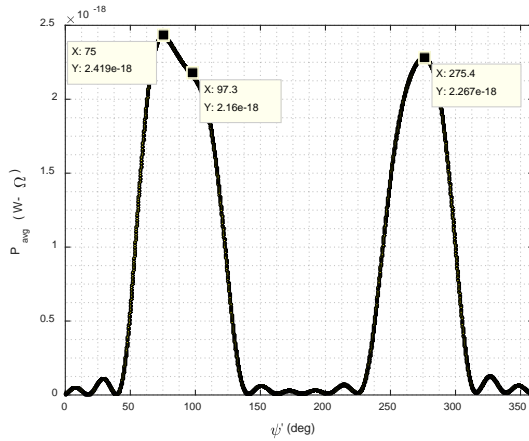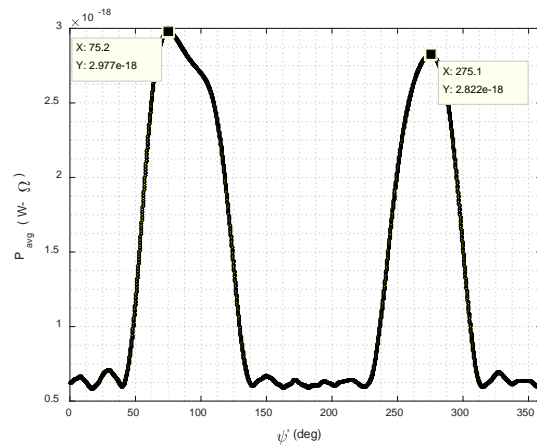
(a)   *(b)*

Figure 34   Time-average power (in W-Ω) of $r(t)$ vs. bearing angle ψ' for the target located at $\psi_S = 75°$, with (a) no noise and (b) SNR = –3 dB.

The time-average power plots for the target located at $\psi_S = 65°$ (Figure 33) show two side peaks, approximately at 105°and 275°. The first one is partially merged with the main peak and has a noticeable correspondence with a sidelobe at about 116° in its FF

74

beam pattern steered to 65°, while the second peak seems to correspond to a small sidelobe at 270° in the beam pattern, as shown in Figure 35(a). For the target located at $\psi_S = 75°$, the correspondence between the time-average power side peak at about 275° and the beam pattern sidelobe at 270°, shown in Figure 35(b), is evident.

Recalling the unexpected side peak at 273° observed in the time-average power plot for the target located at $\psi_S = 55°$—whose corresponding sidelobe in the FF beam pattern was not identified—that peak at 273° seems to correspond actually to a small sidelobe barely visible at 270° in this beam pattern, which evolves to the big sidelobe seen in the beam pattern steered to 75°.

Since the side peak in the time-average power plot for the target located at $\psi_S = 75°$ is almost the same magnitude of the main peak, this could lead to an ambiguity in the estimation of the bearing angle. Therefore, it is more reasonable to set the limit for estimating ψ_S equal to 65°.

(a)   *(b)*

Figure 35   Normalized, horizontal FF beam patterns in the *XY* plane of the twin-line planar array vs. bearing angle ψ, for the carrier frequency 1000 Hz, and beam steered to (a) 65° and (b) 75°.

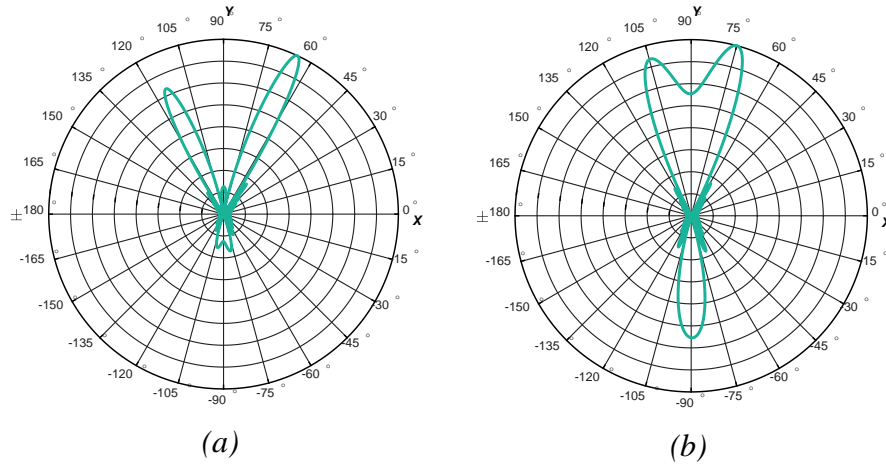## 2. Estimation of the Target's Bearing Angle using the Far-Field Beam Pattern

The normalized, magnitude of the frequency-and-angular spectra $\hat{R}(q, r, s)$ of the twin-line planar array as a function of direction cosines u and v to be discussed in this section were calculated for the operational frequency 1000 Hz, using a time-domain FFT followed by a two-dimensional spatial FFT with both bin spacings δu and δv set to 0.01. As discussed in Chapter V, the magnitude of $\hat{R}(q, r, s)$ is proportional to the FF beam pattern. Therefore, the results obtained in this section from the density plots of the normalized, magnitude of the frequency-and-angular spectra also hold for the FF beam patterns.

Each spectrum $\hat{R}(q, r, s)$ is calculated for the target located at given angular coordinates (θ_S, ψ_S), whose direction cosines (u_S, v_S) are obtained using Equations (4.13) and (4.15), respectively. The direction cosines $(u_{r'}, v_{s'})$ corresponding to the peak of the density plot are determined in the MATLAB code. As discussed in Chapter V, direction cosines $(u_{r'}, v_{s'})$ with no beam steering are the estimates of the target's direction cosines with opposite signs, that is, $(u_{r'}, v_{s'})\big|_{\text{no beam steering}} \equiv (-u_S, -v_S)$, and can be expressed as the estimates $(\hat{\theta}_S, \hat{\psi}_S)$ by using Equations (5.67) and (5.68), respectively.

First the target was located at $(\theta_S, \psi_S) = (90°, 55°)$, which corresponds to $(u_S, v_S) = (0.5736, 0.8192)$. The resulting density plot obtained with no beam steering and no additive noise yields direction cosines $(u_{r'}, v_{s'}) = (-0.5700, -0.8200)$ and corresponding estimates $(\hat{\theta}_S, \hat{\psi}_S) = (87.02°, 55.19°)$, as illustrated in Figure 36. Therefore, in this case the spectrum yields a good estimation of the target's location.

Still referring to the case $(\theta_S, \psi_S) = (90°, 55°)$ and with no noise, Figure 37 shows the density plots corresponding to $\theta' = 90°$ and beam steering angle ψ' equal to 40° (a) and 55° (b). In the case of $\psi' = 55°$, the direction cosines $(u_{r'}, v_{s'})$ obtained from the density plot were equal to (0.0, 0.0), as expected.

76

Figure 36   Normalized, magnitude of the frequency-and-angular spectrum
$\hat{R}(q, r, s)$ of the twin-line planar array vs. direction cosines u and v,
for $f = 1000$ Hz, $(\theta_S, \psi_S) = (90°, 55°)$, with no additive noise and no
beam steering.

(a)   *(b)*

Figure 37   Normalized, magnitude of the frequency-and-angular spectrum
$\hat{R}(q, r, s)$ of the twin-line planar array vs. direction cosines u and v,
for $f = 1000$ Hz, $(\theta_S, \psi_S) = (90°, 55°)$, and no additive noise, steered
to ψ' equal to (a) 40 $°$ and (b) 55 $°$.

For the target located at $(\theta_S, \psi_S) = (90°, 15°)$, which corresponds to $(u_S, v_S) = (0.9659, 0.2588)$, Figure 38(a) shows the density plot with no beam steering and no additive noise, which yielded direction cosines $(u_{r'}, v_{s'}) = (-0.9700, -0.2600)$ and corresponding estimate $\hat{\psi}_S = 15.00°$. Note that in this scenario the angle $\hat{\theta}_S$ could not be estimated, since $\sqrt{(u_{r'})^2 + (v_{s'})^2} = 1.0085$ violates the inequality constraint in Equation (5.67). Simulating additive noise with SNR $= -3$dB and no beam steering yielded the density plot shown in Figure 38(b), with $(u_{r'}, v_{s'}) = (-0.9900, -0.2600)$ and corresponding estimate $\hat{\psi}_S = 14.86°$. Again, the estimate $\hat{\theta}_S$ could not be determined, since $\sqrt{(u_{r'})^2 + (v_{s'})^2} = 1.0477$ also violates the same referred inequality constraint.

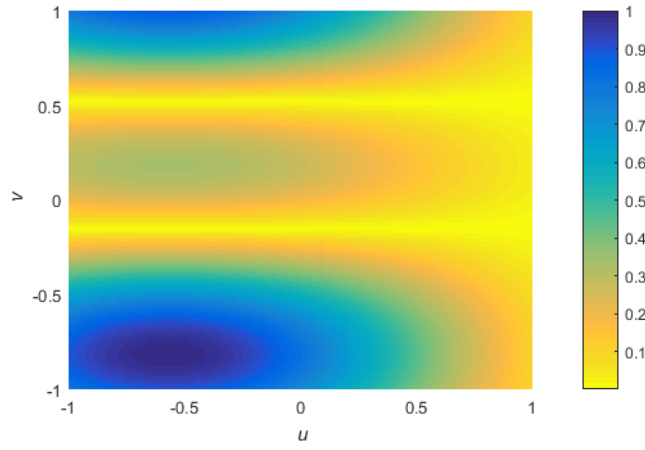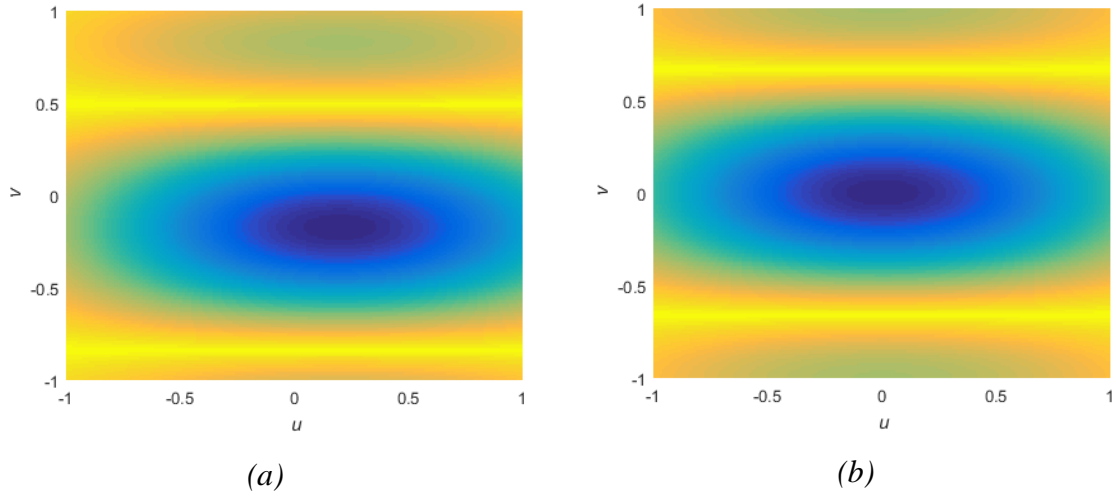(a)   (b)

Figure 38   Normalized, magnitude of the frequency-and-angular spectrum $\hat{R}(q, r, s)$ of the twin-line planar array vs. direction cosines u and v, for $f = 1000$ Hz, $(\theta_S, \psi_S) = (90°, 15°)$, no beam steering, with (a) no noise and (b) additive noise with SNR $= -3$dB.

Setting the target location to $(\theta_S, \psi_S) = (90°, 65°)$, which corresponds to $(u_S, v_S) = (0.4226, 0.9063)$, Figure 39(a) shows the density plot with no beam steering and no additive noise, yielding direction cosines $(u_{r'}, v_{s'}) = (-0.4200, -0.9100)$ and

78

corresponding estimate $\hat{\psi}_S = 65.22°$. The angle $\hat{\theta}_S$ could not be estimated, since $\sqrt{(u_{r'})^2 + (v_{s'})^2} = 1.0045$ violates the inequality in Equation (5.67). Simulating additive noise with SNR = –3dB and no beam steering yielded the density plot shown in Figure 39(b), with $(u_{r'}, v_{s'}) = $ (-0.4300, -0.9000) and corresponding estimates $(\hat{\theta}_S, \hat{\psi}_S) = $ (84.21, 64.46°).

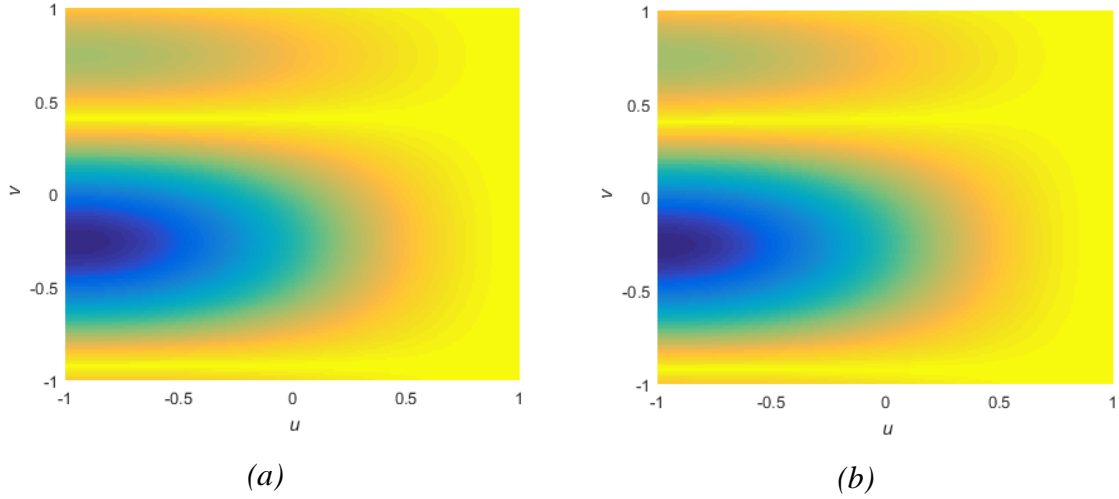(a)   (b)
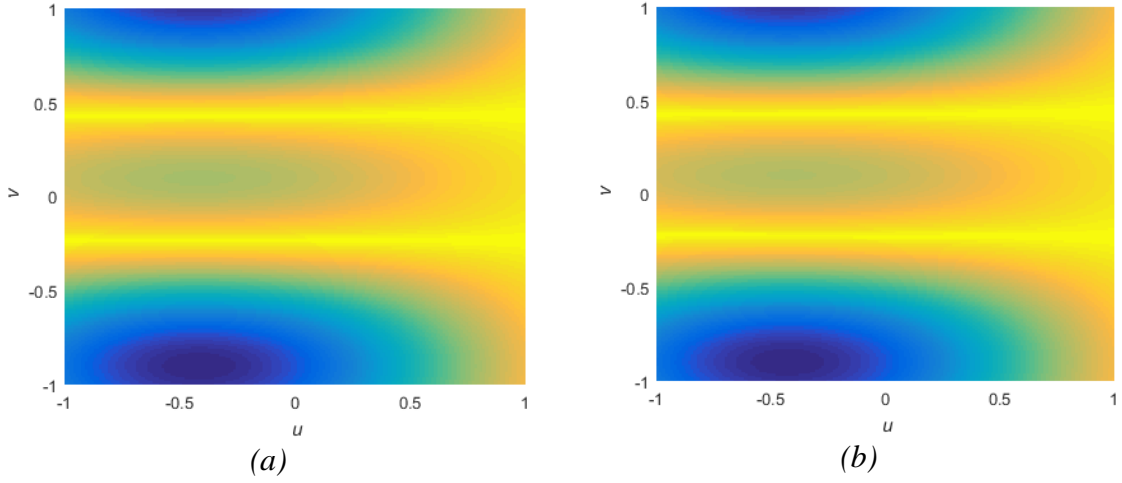
Figure 39   Normalized, magnitude of the frequency-and-angular spectrum
$\hat{R}(q, r, s)$ of the twin-line planar array vs. direction cosines u and v,
for $f = 1000$ Hz, $(\theta_S, \psi_S) = (90°, 65°)$, no beam steering, with (a) no
noise and (b) additive noise with SNR = –3dB.

The estimates of bearing angle ψ_S obtained for the target location (θ_S, ψ_S) at (15°, 90°), (55°, 90°) and (65°, 90°) using the frequency-and-angular spectra $\hat{R}(q, r, s)$ were very close to the actual values. The method failed for estimating the angle θ_S, except for $\theta_S = 65°$ in the presence of noise with SNR = –3dB.

THIS PAGE INTENTIONALLY LEFT BLANK

VII. CONCLUSIONS

A.   SUMMARY

The resolution of port/starboard (PS) ambiguity was investigated for two types of towed sonar arrays, a linear array of triplets and a twin-line planar array, in the frequency range 10–1000 Hz, where significant components of target's acoustic signatures typically are present.

The ability to resolve PS ambiguity in a linear array of triplets is based on the beam pattern of a single triplet. This research used complex weights derived in [9] for a single triplet, which yields a beam pattern with a cardioid shape, ensuring a prominent mainlobe either at starboard or at port side. The radius of the single triplet was determined by using the upper frequency limit of 1000 Hz, and is equal to 250 mm. Throughout the frequency range the single triplet's beam pattern kept the cardioid shape.

The horizontal, far-field beam patterns of a linear array of 11 triplets as a function of frequency were studied. Below 100 Hz the far-field beam pattern of the linear array of triplets looks like the far-field beam pattern of a single triplet. A sharp mainlobe is present in the frequency interval 200–1000 Hz when no beam steering is done, particularly from 600 Hz on. Beam steering reduces the frequency interval where the mainlobe is sharp and free of distortion. The bearing angle steering limit for the tested linear array is 45°, for an optimal operational frequency interval of 600–1000 Hz.

The PS ambiguity rejection in a twin-line planar array is accomplished when its interelement spacings in the X and Y directions are set to ¼ and ½ of the operational wavelength, respectively [9]. Using these criteria, a twin-line planar array with six elements per line was configured using 1000 Hz, yielding a horizontal, far-field beam pattern with a single mainlobe, either on the starboard or port side, when no beam steering was done. This array is 3.75 m long and the two lines are separated by 0.375 m. Any digression from the above criteria led to a progressive loss for the resolution of PS ambiguity. At 500 Hz, significant sidelobes appeared. Segmentation of the twin-line planar array into sub-arrays mitigates this problem, as demonstrated for a 26-element

twin-line planar array configured with three sub-arrays—set to sub-array frequencies 1000, 333.3, and 200 Hz, respectively—each one compliant with the PS rejection criteria.

The FFT beamforming capability of the twin-line planar array was assessed by means of a signal generator, which was designed to provide the array elements with a simulated signal coming from an omnidirectional point-source, propagating through a simple medium. The source radiated a rectangular-envelope, CW (continuous wave) pulse with a carrier frequency of 1000 Hz. The simulated source strength was based on the radiated noise level produced by a modern diesel submarine. The ocean medium was modeled as unbounded, viscous, and homogeneous. Ambient ocean noise and receiver noise were added to the outputs of the elements, simulated as zero-mean sequences from a Gaussian random number generator. The twin-line planar array had the same configuration as that mentioned above, with six elements per line, and used the specifications of a commercial hydrophone as reference for the receiver sensitivity of its sensors. The simulations were performed by setting the target in the same plane as the twin-line planar array, at two different bearing angles. As the beam pattern of the array was steered by varying the bearing steering angle from 0° to 359°, the time-average power of the total output electrical signal from the array was computed. In addition, the normalized, magnitude of the frequency-and-angular spectrum $\hat{R}(q, r, s)$, using a time-domain FFT followed by a two-dimensional spatial FFT was calculated. Results show that both methods (time-average power and frequency-and-angular spectrum) used to estimate the target's bearing angle produced very accurate results, for both no noise and signal plus noise scenarios (SNR = +3 dB, 0 dB and –3dB).

B.   FUTURE WORK

The next step is to employ more realistic models for the ocean medium, include additional targets and jammers, and simulate relative movement between target and array, due to tides in shallow water, target navigation or maneuvers, sensor element vibration due to flow noise, and changes in depth and cable twists during the towing—which also demand additional features for the twin-line planar array module.

The current unbounded and homogenous ocean medium model can be replaced by a model which takes into account interactions with the ocean surface (reflection and Doppler shift due to wave motion) and bottom (reflection and absorption), and the speed of sound as a function of depth, which leads to refraction of sound during propagation. A ray tracing algorithm could be used to calculate the propagation of sound in the medium. In the case of sources radiating at low frequencies, the acoustic pressure in a wave guide model for the medium could be calculated using either normal modes (range-independent speed of sound) or the parabolic equation (PE) method (range-dependent speed of sound) [14]. Alternatively, instead of implementing these models in MATLAB, one can use acoustic channel simulators offered by underwater research institutions, such as the U.S. Office of Naval Research.

Regarding ambient noise, instead of using AWGN (additive white Gaussian noise), one could take theoretical and empirical data and spectra for different types of noise (wind, rain, ship traffic) available in the literature to incorporate into the model. Mathematical equations for receiver noise—both thermal and flow noise are also available. Noise due to vibrations and pressure variations caused by vertical motion could be modeled as AWGN.

Concerning the twin-line planar array, the design could be improved with a means to reduce the interelement spacing in the X direction. The value of d_X dimensioned in this thesis for the operational frequency 1000 Hz—0.375 m—might be too large for the operational limitations discussed in Chapter I .

For the case of simulating moving targets, cable twists and flow noise vibrations, adaptive beamforming could be employed for target tracking. An additional module could be introduced to the system—a detector. Given a specification for the probabilities of detection and false-alarm, and the minimum SNR expected at the output of the array elements for a given target or group of targets, the detection module calculates the required array gain. Based on the array gain, the number of elements of the twin-line planar array is determined.

THIS PAGE INTENTIONALLY LEFT BLANK

APPENDIX. DERIVATION OF THE STANDARD DEVIATION FOR A GIVEN SNR.

$$SNR \text{ (in dB)} \triangleq 10 \log \frac{P_{avg,x}}{P_{avg,z}}$$

$$z(l) = \sigma_z z_o(l), \quad z_o(l) \sim N(m_{z_o}, \sigma_{z_o}^2) = N(0,1)$$

$$P_{avg,z} \triangleq \frac{1}{L} \sum_{l=0}^{L-1} E\left\{|z(l)|^2\right\} = \frac{1}{L}\left(L \times E\left\{|z(l)|^2\right\}\right), \text{ since } z(l) \text{ is assumed to}$$

be a wide-sense stationary (WSS) random sequence

$$P_{avg,z} = E\left\{|z(l)|^2\right\} \triangleq E\left\{z(l) z^*(l)\right\}$$

$$z(l) \text{ is real } \rightarrow P_{avg,z} = E\left\{z(l) z(l)\right\}$$

$$P_{avg,z} = E\left\{\sigma_z z_o(l) \; \sigma_z z_o(l)\right\} = \sigma_z^2 E\left\{z_o(l) \; z_o(l)\right\} \triangleq \sigma_z^2 R_{z_o}(l-l) = \sigma_z^2 R_{z_o}(0)$$

$$R_{z_o}(k) = \sigma_{z_o}^2 \delta(k) = \begin{cases} \sigma_{z_o}^2, & k = 0 \\ 0, & \text{otherwise} \end{cases} \rightarrow R_{z_o}(0) = \sigma_{z_o}^2$$

$$\sigma_{z_o}^2 = 1 \rightarrow P_{avg,z} = \sigma_z^2$$

$$SNR = 10 \log \frac{P_{avg,x}}{P_{avg,z}} = 10 \log \frac{P_{avg,x}}{\sigma_z^2} \rightarrow 10^{SNR/10} = \frac{P_{avg,x}}{\sigma_z^2}$$

$$\sigma_z = \sqrt{\frac{P_{avg,x}}{10^{SNR/10}}} \rightarrow \sigma_z = \sqrt{P_{avg,x}} \; 10^{-SNR/20}$$

THIS PAGE INTENTIONALLY LEFT BLANK

LIST OF REFERENCES

[1] R. J. Urick, "Radiated noise of ships, submarines and torpedoes: Radiated-noise levels," in *Principles of Underwater Sound*, 3rd ed. Westport, CT: Peninsula Publishing, 1983, pp. 332–342.

[2] S. G. Lemon, "Towed-Array History, 1917–2003," *IEEE Journal of Oceanic Engineering*, pp. 365–373, April 2004.

[3] A. Barbagelata, P. Guerrini and L. Troiano, "Thirty Years of Towed Arrays at NURC," *Oceanography*, pp. 24–33, June 2008.

[4] M. Lasky, R. D. Doolittle, B. D. Simmons and S. G. Lemon, "Recent Progress in Towed Hydrophone Array Research," *IEEE Journal of Oceanic Engineering*, pp. 374–387, April 2004.

[5] A. Baldacci and G. Haralabus, "Signal processing for an active sonar system suitable for advanced sensor technology applications and environmental adaptation schemes," in *Signal Processing Conference, 2006 14th European*, 2006.

[6] K. M. Becker and J. R. Preston, "The ONR Five Octave Research Array (FORA) at Penn State." In *OCEANS 2003*, *Proceedings* (Vol. 5), San Diego, 2003.

[7] G. Haralabus and A. Baldacci, "Unambiguous triplet array beamforming and calibration algorithms to facilitate an environmentally adaptive active sonar concept," in *OCEANS 2006*, Boston, 2006.

[8] J. Groen, S. P. Beerens, R. Been, H. Doisy and E. Noutary, "Adaptive port–starboard beamforming of triplet sonar arrays," *IEEE Journal of Oceanic Engineering*, vol. 30, no. 2, pp. 348–359, April 2005.

[9] L. J. Ziomek, *An Introduction to Sonar Systems Engineering*. Boca Raton, FL: CRC Press. In publication.

[10] L. E. Kinsler et al., *Fundamentals of Acoustics*, 4th ed. New York: John Wiley & Sons, 2000, p. 175.

[11] D. Kapolka, "Underwater acoustics for naval applications," course notes for PH3452-Underwater Acoustics, Naval Postgraduate School, Monterey, CA, Winter 2015, p. 90.

[12] X. Lurton, "Transducers and Array Processing" in *An Introduction to Underwater Acoustics, Principles and Applications*. Chichester, UK: Springer/Praxis Publishing, 2002, p. 149.

[13]   Cetacean Research Technology. (n.d.). [Online]. Available:
        http://www.cetaceanresearch.com/hydrophones/c55-hydrophone/index.html.
        [Accessed May 14, 2016].

[14]   A. R. Robinson and D. Lee, *Oceanography and Acoustics*. New York: American
        Institute of Physics, 1994, pp. 8–14.

INITIAL DISTRIBUTION LIST

1.   Defense Technical Information Center
        Ft. Belvoir, Virginia

2.   Dudley Knox Library
        Naval Postgraduate School
        Monterey, California